Technical Report

TR-06-02

Inspection of copper canisters for spent nuclear fuel by means of ultrasound

Synthetic aperture imaging, evaluation of ultrasonic attenuation in copper

Tadeusz Stepinski (editor), Fredrik Lingvall
Erik Wennerström, Ping Wu
Uppsala University, Signals and Systems
Department of Engineering Sciences

January 2006

Svensk Kärnbränslehantering AB
Swedish Nuclear Fuel
and Waste Management Co
Box 5864
SE-102 40 Stockholm Sweden
Tel 08-459 84 00
+46 8 459 84 00
Fax 08-661 57 19
+46 8 661 57 19

Inspection of copper canisters for spent nuclear fuel by means of ultrasound

Synthetic aperture imaging, evaluation of ultrasonic attenuation in copper

Tadeusz Stepinski (editor), Fredrik Lingvall
Erik Wennerström, Ping Wu
Uppsala University, Signals and Systems
Department of Engineering Sciences

January 2006

Abstract

This report contains the research results concerning advanced ultrasound for the inspection of copper canisters for spent nuclear fuel obtained at Signals and Systems, Uppsala University in years 2004/2005.

After a short introduction a new super-resolution synthetic aperture imaging (SRSAI) technique is proposed. The proposed SRSAI is characterized by an excellent lateral resolution and much higher signal to noise ratio compared with ESAFT which was proposed in our previous reports. The ESAFT is based on the assumption that probability density of the imaged targets (so called prior) is Gaussian, which is the simplest case for the analysis. The increased performance of SRSAI is due to more realistic assumption concerning probability density function of targets in the region of interest. It is shown, both using simulations and in an experiment that if the target reflectivity is assumed to be positive a substantial increase of resolution and signal to noise ratio in the reconstructed image can be obtained.

In the second chapter the result of the evaluation of ultrasonic attenuation in copper blocks with different grain size is presented. A short presentation of basic theory of the buffer-rod and the immersion methods is given in the beginning (the detailed derivation is provided in the appendix). Then the measurement setup and copper specimens are specified and the results of measurements made on copper specimens are presented. Correlation between the attenuation and grain size for the inspected specimens is discussed.

Contents

Chapter 1

Introduction

by Tadeusz Stepinski

1.1 Outline of the Report

Reliable detecting and sizing natural defects in EB and friction stir welds that will be used for sealing copper canisters for spent nuclear fuel requires applying advanced ultrasonic imaging techniques. In this report we are presenting our recent results concerning inspection of copper canisters for spent nuclear fuel by means of ultrasound.

Our research activity in this project in year 2004/2005 which is presented in this report was split in two separate tasks:

- Synthetic aperture imaging, and
- NDE of grain size in copper

The first task, which is a continuation of our experimental and theoretical research concerning synthetic aperture imaging and its NDE applications is reported in Chapter 2. We are presenting a new super-resolution synthetic aperture imaging (SRSAI) technique, which is characterized by an excellent lateral resolution and much higher signal to noise ratio than the extended synthetic aperture focusing technique (ESAFT) that was proposed in our previous reports.

The superior performance of SRSAI is due to the application of a more realistic assumption concerning probability density function of targets in the region of interest than the Gaussian model assumed in ESAFT. In the SRSAI it is assumed that the targets have always a positive reflectivity characterized by the exponential distribution. This assumption leads to a quadratic optimization problem with inequality constraints which is solved using an iterative algorithm.

It is shown, both using simulations and in an experiment that a substantial increase in resolution and signal to noise ratio in the reconstructed image can be obtained using SRSAI compared with ESAFT.

The second task, concerned with nondestructive characterization of copper material used for canisters, which was started in 2003 has now been completed and is reported in Chapter 3. The contents of this task has been modified after achieving first experimental results and drawing preliminary conclusions. The original intention was to develop methods for grain size evaluation in copper material using ultrasound. It appeared, however, that defect detectability using ultrasound is more correlated with ultrasonic attenuation than the grain size. Therefore, the research has been focused on methods for reliable estimation of ultrasonic attenuation as well as defect detectability.

In Chapter 3 we present the buffer-rod method (BRM) and the immersion method (IM) that yield objective values of ultrasonic attenuation in solid materials irrespective of the setup used in the measurement. Short presentation of basic theory of the buffer-rod and the immersion methods is given in the beginning of the Chapter (the detailed derivation is provided in the appendix). A solution to the problem of automatic compensation of transducer diffraction effects is presented. Description of the measurement setup and copper specimens is given in the sequel. The measurements on copper specimens were carried out in immersion using two ultrasonic instruments, the Allin system, and the RITEC instrument, the latter was used as a reference.

The effect of grain size on the defect detectability was investigated by imaging quasi-flat bottom holes (FBHs) of different diameters made in copper specimens with different grain size. The SNR estimated for holes echoes were analyzed in terms of both grain size and attenuation. The results demonstrate that the SNR is stronger correlated with the evaluated ultrasonic attenuation in the respective blocks than with their grain size.

Chapter 2

Synthetic Aperture Imaging

by Fredrik Lingvall and Erik Wennerström

2.1 Introduction

The aim of this chapter is to report our recent results of experiments and simulations concerning the synthetic aperture imaging (SAI) and the parallel array imaging (PAI). The following issues are addressed in this chapter:

- effects of finite-sized transducers and sparsely sampled or under-sampled arrays on SAI,
- parallel array imaging including presentation of Bayesian estimators.

The experiments presented here have been conducted using a array system and a standard immersion tank. The broadband data were acquired using a 1D array, employing both electronic and mechanical scanning. To make the reconstruction results easy to interpret, wire targets immersed in water were used. The simulations in this chapter were designed to emulate the physical array system. This was done in order to facilitate the comparison with the experimental data.

For practical reasons, all investigations, both experimental and simulated, have been conducted on two-dimensional data only. In this way the memory and CPU requirements are reduced. Note however, that from the theoretical point of view there are no hinders to implement the Bayesian methods discussed here to full 3D data.

This chapter is organized as follows: In section 2.2, the array system used for the measurements is described. This section also contains a short description of how the SAI and the parallel imaging experiments have been conducted. Section 2.3 describes the SAI experiments, for investigation of the lateral resolution, when using finite-sized transducers. In Section 2.4, the parallel array experiments are discussed. Topics treated are grating lobe suppression and estimation performance, both with respect to different focusing methods and to signal-to-noise ratios. This section includes a comparison of the delay-and-sum (DAS), matched filter, and the linear minimum mean-square error (MMSE) methods as well as the non-linear maximum a posteriori (MAP) estimator. In Section 2.5, the solution to the parallel imaging with exponential *a priori* probability of scattering amplitudes is presented. Finally, in Section 2.6, the results are summarized and conclusions are given.

2.2 Experimental Equipment

The experimental data for this chapter were acquired using an ALLIN array system manufactured by NDT Systems. This system is equipped with an electronic beamformer that allows for focusing in both the transmit and the receive operation. The driving unit can use a maximum of 32 elements simultaneously, but only with 16 unique focusing delays, and beam steering can therefore only be performed using 16 elements. The system has an analog multiplexer that controls which array inputs are connected to the 8-bit analog-to-digital converter (ADC).[1]

Since the data, can be acquired using the analog multiplexer, which electronically connects successive array elements, a very fast scanning of the beam is possible. The system can also perform mechanical scanning using a motor controlled robot.

In the first experiment, in section 2.3.2, the ALLIN system was connected to a 32 element concave 1D array designed for immersion testing, manufactured by Imasonic (see Fig. 2.1). This array has a dimension of 32×24 mm, where each individual element is 0.9×24 mm. Each array element is geometrically focused in the y-direction at the depth $z = 80$ mm. The array pitch, d, is 1 mm and the elements are thus separated by 0.1 mm. The array has a center frequency

---

[1] The 8-bit ADC limits the dynamic range of the system to 48 dB.

at approximately 3 MHz which corresponds to $\lambda = 0.5$ mm in water. The array pitch is then approximately 2λ and the array is under-sampled according to the array sampling theorem.

In all other experiments, the ALLIN system was connected to a similar 3 MHz array from Imasonic, with 64 0.9×33.5 mm elements geometrically focused at 190 mm.

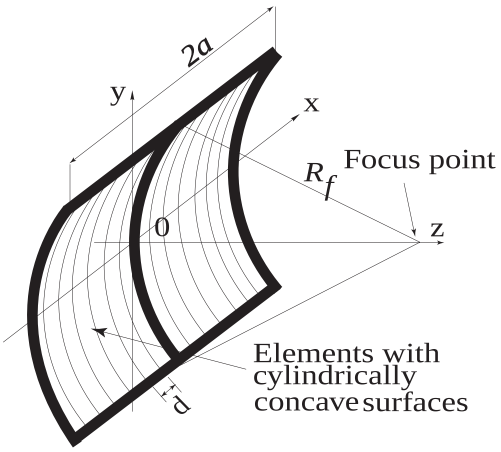

(a) Geometry of the concave 1D array

(b) The 32 element concave Imasonic array

Figure 2.1: Concave array used in the experiments. (a) Geometry of the concave 1D array. (b) The 32 element concave Imasonic array.

Figure 2.1(a) shows a schematic view of the concave arrays and a photograph of the 32-element Immasonic array.

This system was used in experiments for both synthetic aperture imaging (SAI) and parallel array beamforming. The SAI experiments were performed using different numbers of active array elements that were bridged together to form apertures mimicking single transducers with different sizes but with almost identical electrical characteristics. The apertures were then scanned over targets with a mechanical XY scanner. This measurement method facilitates the comparison of SAI experiments with different transducer sizes since the electrical impulse responses are the same regardless of the transducer size.

A parallel beamformer (also referred to as total focusing method (TFM)) uses multiple focusing laws to beamform at many points simultaneously. To acquire data for parallel imaging, the received signals from all elements must be available. Since the ALLIN system only has one ADC, parallel beamforming experiments cannot be performed from data acquired using a single emission. A parallel data acquisition can, however, be emulated by using the analog multiplexer to sequentially acquire signals from each element with the array at the same position. All parallel array imaging experiments have been conducted using this technique.

2.3 Ultrasonic Synthetic Aperture Imaging

In this section the specific effects due to transducer element size have been studied. SAI experiments were carried out using a number of bridged array elements that simulated a variable size transducer that could be shifted without restrictions using the XY scanner. The experiments were performed in a monostatic mode, which means that the same aperture was used for transmitting and receiving ultrasonic signals.

Below, we present the propagation matrix for monostatic SAI.

2.3.1 The Monostatic Propagation Matrix

The propagation matrix developed in [1, 2] was derived for a general measurement setup, allowing for transmission and reception using arbitrary combinations of transducers. Cylindrical concave transducer, symmetric with respect to XZ plane was used in the SAI experiments presented in this report. In this case the acoustic transmit and reception processes will be identical, that is, the transmit and receive spatial impulse responses (SIRs) will be the same. Also the double-path SIRs associated with observation points that are located symmetrically with respect to the XZ plane will be identical.

The A-scan signal, $\mathbf{y}_n$, received by a transducer at x_n, is given by:

$$\mathbf{y}_n = \sum_{\tilde{n}=0}^{N-1} \mathbf{P}_{d(\tilde{n},n)} \mathbf{o}_{\tilde{n}} + \mathbf{e}_n. \tag{2.1}$$

where $\mathbf{P}_{d(\tilde{n},n)}$ is the $M \times N$ propagation matrix defined for the A-scan $\mathbf{y}_n$ obtained at the horizontal distance $d(\tilde{n}, n)$ between the observation point at $x_{\tilde{n}}$, and the horizontal transducer position x_n. Due to the symmetry of the transducer, the $\mathbf{P}_{d(\tilde{n},n)}$ matrices for vertical lines at the same horizontal distance from the transducer will be identical, that is,

$$\mathbf{P}_{d(n-i,n)} = \mathbf{P}_{d(n+i,n)} \tag{2.2}$$

for an integer i in the region of interest (ROI).[2] Moreover, the matrix $\mathbf{P}_{d(\tilde{n},n)}$ is also invariant with respect to a parallel shift of the position of the transducer, in the sense that

$$\mathbf{P}_{d(\tilde{n}+i,n+i)} = \mathbf{P}_{d(\tilde{n},n)}. \tag{2.3}$$

Furthermore, the number of elements in the propagation matrix can be decreased by noting that the contributions for observation points at large distances from the transducer will be small due to the limited lobe width of the transducer.

Therefore, the summation in (2.1) can be truncated without introducing any significant errors. That is, (2.1) can be simplified to

$$\mathbf{y}_n \approx \sum_{\tilde{n}=n-\tilde{L}/2}^{n+\tilde{L}/2} \mathbf{P}_{d(\tilde{n},n)} \mathbf{o}_{\tilde{n}} + \mathbf{e}_n, \tag{2.4}$$

---

[2] It is assumed that the ROI is spatially sampled at regular intervals.

where $\tilde{L}$ is the number of transducer positions that significantly contribute to the response from targets located along the vertical line at $x_{\tilde{n}}$.

Using (2.4), and the symmetries (2.2) and (2.3), the total propagation matrix for monostatic SAI imaging can finally be expressed,

$$\mathbf{P} = \begin{bmatrix} \mathbf{P}_{d(i-\tilde{L}/2,i)} & \cdots & \mathbf{P}_{d(i+\tilde{L}/2,i)} & & & \\ & \mathbf{P}_{d(i-\tilde{L}/2,i)} & \cdots & \mathbf{P}_{d(i+\tilde{L}/2,i)} & & \mathbf{0} \\ & & \ddots & & \ddots & \\ \mathbf{0} & & & & & \\ & & & \mathbf{P}_{d(i-\tilde{L}/2,i)} & \cdots & \mathbf{P}_{d(i+\tilde{L}/2,i)} \end{bmatrix}, \tag{2.5}$$

for any i such that $i - \tilde{L}/2$ and $i + \tilde{L}/2$ is in the ROI.

If the length of the A-scans, $\mathbf{y}_n$, is K then for $\tilde{L}$ transducer positions the size of the propagation matrix (2.5) is a $K\tilde{L} \times MN$.

2.3.2 Lateral Resolution and Finite Sized Transducers

A deficiency of the SAFT method comes from treating the scanning transducer as a point source. This results in a mismatch of the SAFT filter if the transducer has a finite size [1].

To study only the influence of the transducer size on the lateral resolution, a simplified propagation matrix, $\mathbf{P}_{\text{SIR}}$, can be used which only contains the double-path SIRs and not the electrical impulse responses. This essentially assumes the propagation model

$$\mathbf{y} = \mathbf{P}_{\text{SIR}}\mathbf{o} + \mathbf{e} \tag{2.6}$$

where $\mathbf{P}_{\text{SIR}}$ has the same structure as the propagation matrix, $\mathbf{P}$ in (2.5) but does not include the electrical impulse responses.

The filter matrix in the ESAFT estimator is given by [1, 2]

$$\mathbf{K}_{MMSE} = \mathbf{C}_{\text{o}}\mathbf{P}_{\text{SIR}}^T(\mathbf{P}_{\text{SIR}}\mathbf{C}_{\text{o}}\mathbf{P}_{\text{SIR}}^T + \mathbf{C}_{\text{e}})^{-1}. \tag{2.7}$$

where $\mathbf{C}_{\text{o}}$ and $\mathbf{C}_{\text{e}}$ are the covariance matrices of the reconstructed image $\mathbf{o}$ and measurement errors $\mathbf{e}$, respectively.

Since the model (2.1) does not include the electrical impulse response, the filter (2.7) will only compensate for the specific diffraction effects due to the finite size of the active area of the transducer.

Below experiments using wire targets immersed in water are presented. The experiments were designed such that transducer size effects was apparent.

Experiment 1: Wire Targets

In this experiment, the lateral resolution for the ESAFT estimator (2.7) was evaluated on measured data, and compared to SAFT processing using the same synthetic aperture.

The data were acquired using the 32 element Imasonic array imaging a wire target[3] at $z = 80$ mm. The array was mechanically scanned along a line, and the data were acquired with a pitch $d = 1$ mm and a temporal sampling period, T_{s}, of 0.025 μs (=40 MHz). See figure 2.2. The synthetic aperture consisted of 31 A-scans for both the SAFT and the ESAFT algorithm.

---

[3] A steel pin with a diameter, d, of 0.3 mm was used.

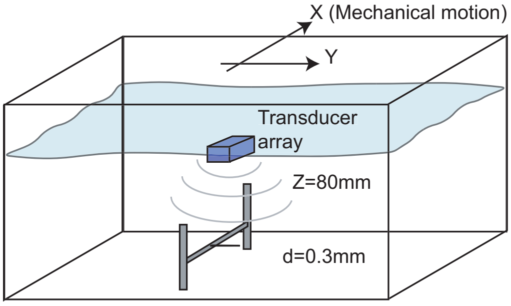

Figure 2.2: Measurement setup.

Two transducer sizes were considered: 4 mm and 16 mm, respectively. They were obtained by firing 4 or 16 elements of the Imasonic array simultaneously. The SIRs associated with the concave array, $\mathbf{S}_{\text{SIR}}$, used in (2.7), were computed using the DREAM toolbox [3].

Furthermore, in all experiments and simulations presented, the following is assumed:

Assumption 1. *The matrices* $\mathbf{C}_o$ *and* $\mathbf{C}_e$ *are assumed to have the form of unity matrices with equal elements,* $\mathbf{C}_o = \sigma_o^2\mathbf{I}$ *and* $\mathbf{C}_e = \sigma_e^2\mathbf{I}$*, respectively.*

The above assumption states that the elements in both $\mathbf{o}$ and $\mathbf{e}$ are uncorrelated, which is reasonable if we do not have any information that indicates any dependence between the elements in $\mathbf{o}$ and $\mathbf{e}$. Using this assumption (2.7) is simplified to

$$\mathbf{K}_{\text{MMSE}} = \mathbf{P}_{\text{SIR}}^T(\mathbf{P}_{\text{SIR}}\mathbf{P}_{\text{SIR}}^T + \sigma_{\text{e}}^2/\sigma_{\text{o}}^2\mathbf{I})^{-1}. \tag{2.8}$$

The ratio $\mu = \sigma_{\text{e}}^2/\sigma_{\text{o}}^2$ was simply used as a tuning parameter, and it was adjusted manually to obtain the best visible performance.

The unprocessed data and the reconstruction results are shown in Figure 2.3. Figures 2.3(a) and (b) show the unprocessed B-scan data, corresponding to the 4 mm and the 16 mm transducer, respectively. The B-scan for the 4 mm transducer has the typical hyperbolic shape associated with small transducers that emit nearly spherical waves. The B-scan from 16 mm transducer, shown in Figure 2.3(b), shows, however, strong effects due to the narrow lobe of its beam pattern and it is clear that the 16 mm transducer cannot be considered as a point source at that distance.[4]

2.3.3 Discussion

The reconstruction results for the SAFT processed 4 mm data, presented in Figure 2.3(c), show a significant improvement in lateral resolution compared to the unprocessed data. However, the SAFT reconstructed image for the 16 mm transducer, shown in Figure 2.3(d) shows no improvement in lateral resolution compared to the unprocessed data. That is, SAFT performance deteriorates when the transducer size increases.

The ESAFT reconstructions, shown in Figures 2.3(e) and (f), demonstrate, on the other hand, high lateral resolution for both transducer sizes. Thus, the ESAFT estimator has successfully compensated for the diffraction effects of the transducer.

One can also finally note that the temporal, or range resolution, is roughly the same in the unprocessed B-scan data and the SAFT processed images. This was expected since the conventional SAFT algorithm does not compensate for the temporal waveform.

---

[4] At far field even large sized transducers can be approximated as point sources.

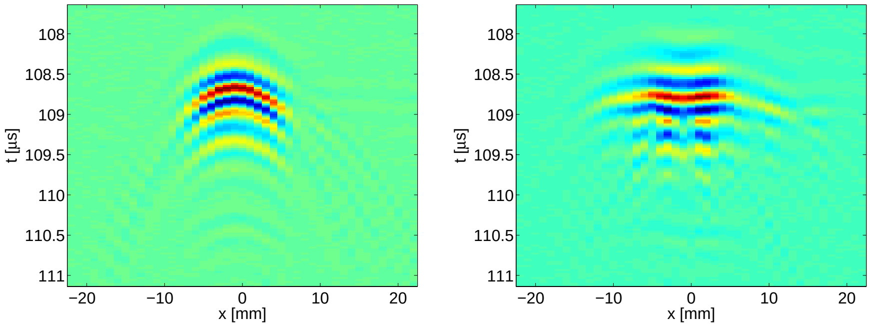

(a) Unprocessed B-scan data: 4 mm transducer.

(b) Unprocessed B-scan data: 16 mm transducer.

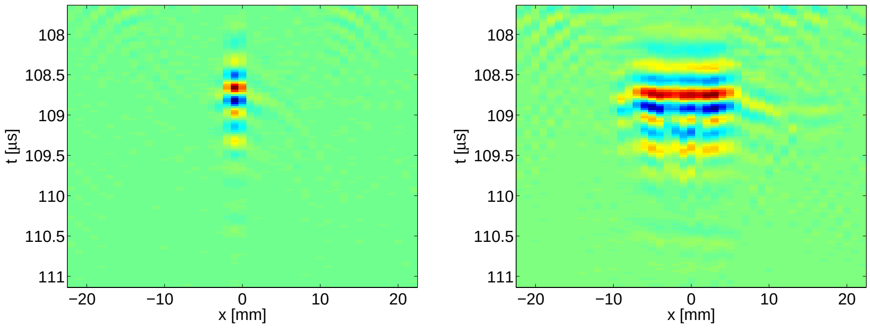

(c) SAFT processed data: 4 mm transducer.

(d) SAFT processed data: 16 mm transducer.

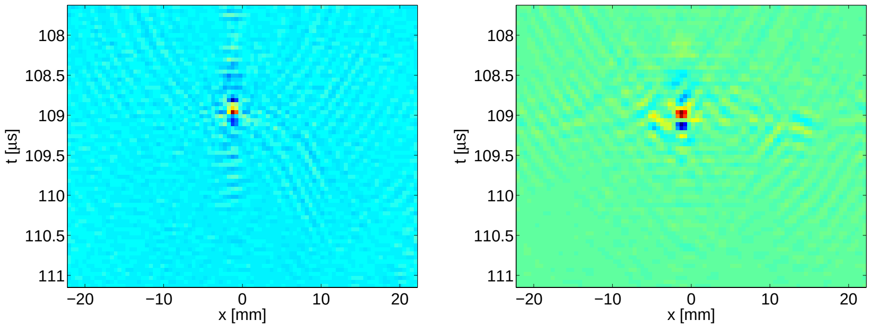

(e) ESAFT processed data: 4 mm transducer.

(f) ESAFT processed data: 16 mm transducer.

Figure 2.3: Comparison between the SAFT and the ESAFT estimator, (2.7), on ultrasonic data from a wire target (steel pin with a diameter of 0.3 mm) at $z = 80$ mm using a phased array.

It is evident from the Experiments above, that the EASFT method can successfully compensate for the size effects of a finite-sized transducer yielding a significantly improved lateral resolution compared to the SAFT based on delay and sum processing only. Thus, the ESAFT method enables more flexible measurement setups since transducers with larger active areas can be used without loosing too much resolution.

2.4 Parallel Array Imaging

In parallel beamforming a number DAS filters are used in parallel to focus the array simultaneously at many points on data received from a single transmission [4–6]. The advantage of this approach is an increased frame rate compared to, for example, sweep beam imaging which requires many transmissions.[5] Typically, a wider then normal transmitted beam is used and a few lines of the total ROI are then reconstructed using parallel receive beamforming [5]. The complete ROI could, in principle, be reconstructed from one transmitted pulse provided that the transmitted beam is wide enough to sufficiently illuminate the ROI. There are, however, practical considerations that make very wide beam illumination difficult. Firstly, it may be difficult to generate a sufficiently wide beam, and secondly, ghost responses due to the grating lobes are stronger for DAS beamformed images when a wide beam is used compared to those present when a sweeped narrow beam [7] is used.

As we will show below, model based reconstruction methods can alleviate some of the above mentioned problems since they can take both the transmission and reception processes into account and compensate for practically any beampattern. The reconstruction methods discussed in this report that are based on the impulse response method, can in principle compensate for grating lobes or any other beampattern, provided that the corresponding spatial impulse responses can be computed.

Below, we will study the linear MMSE estimator and the non-linear MAP estimator with exponential prior in a situation where the array is undersampled. This is done to focus the attention on the lobe aliasing problems that are often apparent in such situations.

2.4.1 The Propagation Matrix for Parallel Receive Imaging

In ordinary phased array imaging the beam is focused or steered in transmission by applying suitable delays to the signals driving individual array elements. The applied delays will then also delay the forward SIRs for each array element, which will result in difference in the forward and backward SIRs. Therefore, the monostatic SAI model 2.1 defined in section 2.3 where the transmit and receive SIRs were identical is not valid any longer in this case.

The system impulse response $h^{\text{sys}}(\mathbf{r},t)$ for the nth receive element can be computed as a superposition of delayed SIRs of all P transmitting elements convolved with the SIR for the nth receive element and its electrical impulse response.

$$h^{\text{sys}}(\mathbf{r},t) = \underbrace{\left(\sum_{p=0}^{P-1} h_p^{\text{f}}(\mathbf{r},t) * \delta(t-\tau_p)\right)}_{\text{total forward SIR}} * \underbrace{h_n^{\text{b}}(\mathbf{r},t)}_{n\text{th backward SIR}} * h_{\text{e}}(t), \tag{2.9}$$

where P in the number of transmitting elements and τ_p is the focusing delay corresponding to the pth transmit element. The received discrete waveform, from a target at an observation

---

[5] Please note however, that parallel beamforming performs focusing in reception only, while the sweep beam technique performs focusing both in transmission and reception.

$(x_m, z_{\tilde{n}})$, can then be expressed as

$$\mathbf{y}_n = \mathbf{h}_m^{(\tilde{n},n)}(\mathbf{O})_{m,\tilde{n}} \tag{2.10}$$

where the vector $\mathbf{h}_m^{(\tilde{n},n)}$ is the discrete system impulse response for the nth receive element.

Similarly to (2.1) the noise corrupted received discrete waveform can be expressed as

$$\begin{aligned}\mathbf{y}_n &= \sum_{\tilde{n}=0}^{N-1} \mathbf{P}_{d(\tilde{n},n)}\mathbf{o}_{\tilde{n}} + \mathbf{e}_n \\ &= \left[\mathbf{h}_0^{(0,n)} \quad \mathbf{h}_1^{(0,n)} \quad \cdots \quad \mathbf{h}_{M-1}^{(0,n)} \quad \mathbf{h}_0^{(1,n)} \quad \cdots \quad \mathbf{h}_{M-1}^{(N-1,n)}\right]\mathbf{o} + \mathbf{e}_n \\ &= \mathbf{P}_n\mathbf{o} + \mathbf{e}_n,\end{aligned} \tag{2.11}$$

and, by appending the received signals from all L receive elements, the total array imaging system can finally be modeled as

$$\begin{aligned}\mathbf{y} = &\begin{bmatrix}\mathbf{P}_0 \\ \mathbf{P}_1 \\ \\ \vdots \\ \mathbf{P}_{L-1}\end{bmatrix}\begin{bmatrix}\mathbf{o}_0 \\ \mathbf{o}_1 \\ \\ \vdots \\ \\ \mathbf{o}_{N-1}\end{bmatrix} + \begin{bmatrix}\mathbf{e}_0 \\ \mathbf{e}_1 \\ \\ \vdots \\ \mathbf{e}_{L-1}\end{bmatrix} \\ =&\mathbf{P}\mathbf{o} + \mathbf{e}.\end{aligned} \tag{2.12}$$

The $KL \times MN$ propagation matrix, $\mathbf{P}$, in (2.12) now describes both the focused transmission process and the reception for an arbitrary focused array.

Note that the model (2.12) is valid for *any* transmit and receive aperture, provided that the corresponding receive and transmit SIRs can be computed. The model (2.12) is therefore not restricted to using the same elements both in receive and transmit, and it can be used to model both dense- and sparse, or under-sampled, arrays.

2.4.2 The Optimal Linear Estimator

The optimal linear estimator can for an array layout can now be found by inserting the propagation matrix from (2.12) into the linear MMSE estimator, $\mathbf{K}_{\text{MMSE}}$, given by [2]

$$\begin{aligned}\mathbf{K}_{\text{MMSE}} &= \arg\min_{\mathbf{K}} \ \mathrm{E}\{\|\mathbf{o} - \mathbf{K}\mathbf{y}\|^2\} \\ &= \arg\min_{\mathbf{K}} \ \mathrm{E}\{(\mathbf{o} - \mathbf{K}\mathbf{y})^T(\mathbf{o} - \mathbf{K}\mathbf{y})\} \\ &= \arg\min_{\mathbf{K}} \ \mathrm{tr}\{\mathbf{C}_{\text{o}}\} - 2\,\mathrm{tr}\{\mathbf{K}^T\mathbf{C}_{\text{o}}\mathbf{P}^T\} + \mathrm{tr}\{\mathbf{K}\mathbf{P}\mathbf{C}_{\text{o}}\mathbf{P}^T\mathbf{K}^T\} \\ &\quad + \mathrm{tr}\{\mathbf{K}\mathbf{C}_{\text{e}}\mathbf{K}^T\}\end{aligned} \tag{2.13}$$

In the experiments performed here a simplified form of (2.13) has been used were the MMSE filter matrix, $\mathbf{K}_{\text{MMSE}}$, for the estimator was computed using Assumption 1. Using this assumption (2.13) reduces to

$$\mathbf{K}_{\text{MMSE}} = \mathbf{P}^T(\mathbf{P}\mathbf{P}^T + \mu\mathbf{I})^{-1}, \tag{2.14}$$

where $\mu = \sigma_{\text{e}}^2/\sigma_{\text{o}}^2$.

The μ parameter in (2.14) is related to the "confidence" that the MMSE estimator has to the data. If the noise is very large then μ will also be large and the factor $\mu\mathbf{I}$ will dominate the inverse $(\mathbf{PP}^T + \mu\mathbf{I})^{-1}$ in (2.14). For very large $\mu \to \infty$ the MMSE estimator will reduce to $\mathbf{P}^T/\mu$. The gain of the MMSE estimator decreases when σ_e^2, and μ, increase. Furthermore, the estimate will tend toward zero, which is the *a priori* mean value of $\mathbf{o}$. In other words, in this case, the measurement vector $\mathbf{y}$ contains no new information about $\mathbf{o}$ and the estimate is only based on our prior information.

For the opposite case, when μ approaches zero, the MMSE estimator (2.14) reduces to $\mathbf{P}^T(\mathbf{PP}^T)^{-1}$. This will however rarely be the case, since uncertainties in the model are always present, thus, we need to set μ to a positive value.[6] Below, we will study the performance of the MMSE estimator and the influence of the μ parameter in the case of distinct grating lobes.

2.4.3 Grating Lobe Suppression of the Optimal Linear Estimator

A very important factor that can severely deteriorate image quality in traditional DAS beamforming is the presence of grating lobes. To evaluate the MMSE estimator (2.14) with respect to grating lobe suppression, measurements and simulations were performed using the setup shown in Figure 2.4. A steered array configuration was chosen since by steering the array beam, the grating lobes will also be steered and therefore will be very well pronounced. The measurements were performed in water using the 64-element Imasonic array whose center frequency is approximately 3 MHz which corresponds to a acoustical wavelength of 0.5 mm in water. Since the array pitch was 1 mm the array was under-sampled. A snapshot of the acoustic field simulated with the DREAM method for a 16 element steered array setup is shown in Figure 2.5.[7] The snapshot was taken slightly before the pulse reached the focal point at approximately (x = -18 mm, z=50 mm). The acoustic energy in the region around x = 8 mm is due to the grating lobe of the under-sampled array. This can also be seen as the peak at x = 8 mm in the profile plot shown in Figure 2.5(b).

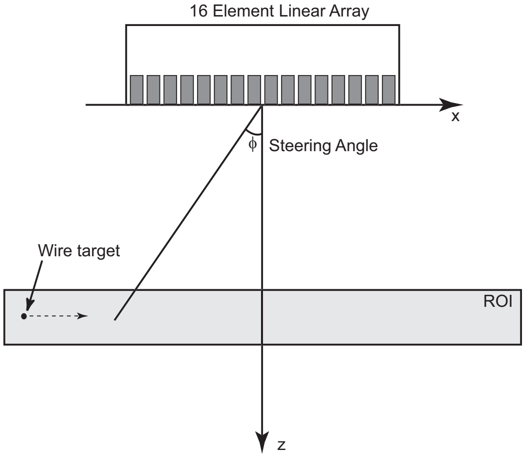

Figure 2.4: Illustration of the measurement setup used in the grating lobe suppression experiments. A 16-element aperture of the 64-element Imasonic array was focused at z = 50 mm and steered with -20°.

From Figure 2.5 it can be seen that the focal point is as predicted at z=50 mm, $x \approx$ -18 mm and a distinct grating lobe at an angle of approximately 10° can be observed due to the fact that the element spacing is larger than $\lambda/2$.

---

[6] Remember that the noise, $\mathbf{e}$, is a combination of all errors of the model (2.12), including measurement noise and model errors.

[7] The under-sampled Allin array setup was simulated.

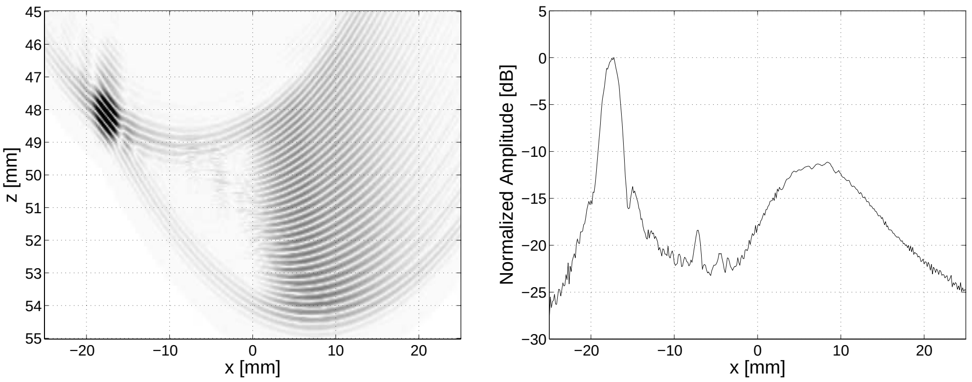

(a) Wave field snapshot at t = 37.3 μs. **(b)** Profile plot of the wave field.

Figure 2.5: Snapshot of the acoustic field at -25 mm $< x <$ 25 mm, 45 mm $< z <$ 55 mm for an aperture consisting of 16 0.9 mm wide elements with array pitch of 1 mm. The aperture was focused at z = 50 mm and steered with -20°.

To study the behavior of the MMSE method, simulated data were obtained by using the linear model (2.12) were the measurement error vector $\mathbf{e}$ was simulated as white noise with Gaussian amplitude distribution. The SNR used in the simulations below was defined as

$$\eta \triangleq \frac{\mathbf{y}^T\mathbf{y}}{\mathbf{e}^T\mathbf{e}}, \tag{2.15}$$

where the signal energy, $\mathbf{y}^T\mathbf{y}$, computed using (2.12) with $\mathbf{e} = 0$, is given by

$$\mathbf{y}^T\mathbf{y} = \mathbf{o}^T\mathbf{P}^T\mathbf{P}\mathbf{o}. \tag{2.16}$$

Thus, the signal energy, $\mathbf{y}^T\mathbf{y}$, is the total energy received by all array elements. Note that the received signal energy, when imaging a single point target, will depend on the position of the target. The SNR will therefore also be a function of the target position and, consequently, the SNR will be low when the target is in the regions illuminated with low acoustic energy and high when the target is in the main or the grating lobe.

Experiment 1: Illustration of Grating Lobe Suppression of the MMSE Estimator

In the first experiment we consider the beamforming performance at the vertical image line where the focal point resides. Ideally, if a target is horizontally moved from the left to right side under the array, cf. Figure 2.4, the reconstructed scattering amplitudes at that line should be zero for all target positions except for that one where the target position and the position of the image line coincides. Normally, due to the finite lobe width and the presence of side- and grating lobes the image will be more complex. The effect of energy leak between the lobes will be observed resulting in ghost responses and a loss in resolution and image contrast.

Figure 2.6(a) shows the results for a simulated 16 element array, and Figure 2.6(b) shows the corresponding results for data measured with the Imasonic array in the setup shown in Figure 2.4. The max amplitudes of the beamformed images at the line corresponding to the main lobe position, x = -18 mm, were plotted as a function of the target position. The DAS beamformer used a fixed receive focus at (z=50 mm, $x = -18$ mm), and the optimal filters for the corresponding image line were used in the MMSE estimator. In the simulations, the noise

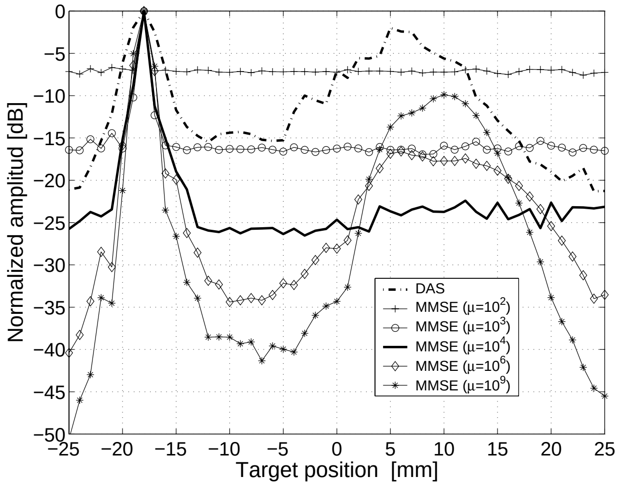

(a) Results for simulated data (SNR= 15.8 [dB]).

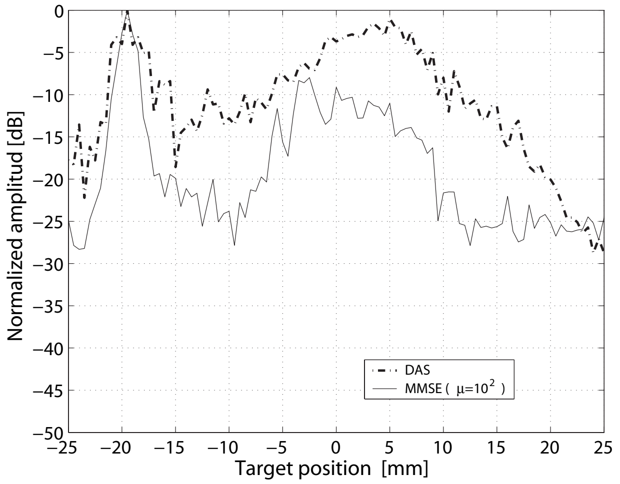

(b) Results for measured data using the Imasonic array and a 0.3 mm wire target.

Figure 2.6: Normalized maximum amplitude as a function of horizontal target position for a 16 element 1D array focused at z =50 mm and steered at an angle of -20°. The point target was located at depth $z = 50$ mm and the SNR in (a), for the target at $x = -18$ mm, was 15.8 dB.

power was constant for all target positions where the SNR, defined by (2.15), was 15.8 dB when the target was at the focal point.

To show the influence of μ in (2.14), when μ is treated as a tuning parameter, the max amplitude was plotted as a function of the position of a unit area point target for five values of μ: $\mu = 10^2$, 10^3, 10^4, 10^6, and 10^9, respectively, see Figure 2.6(a). For low values of μ the MMSE filter relies strongly on the measured data, resulting in a significant noise amplification. This is seen in Figure 2.6(a), for $\mu = 10^2$, where the noise floor only is about 7 dB lower than the maximum amplitude at the focal point. Increasing μ lowers the noise sensitivity but it also results in a worse suppression of the grating lobe, which can be seen for $\mu = 10^6$ and $\mu = 10^9$. A good trade-off between the noise sensitivity and grating lobe suppression is in this case $\mu = 10^4$ where the noise and grating lobe levels are roughly 25 dB lower than the target signal. Note that the MMSE beamformer suppressed the grating lobe better than the DAS does for all the examined μ values. Also, the MMSE reconstructed image has higher lateral resolution than the DAS beamformed one.

A similar behavior can be seen in the experimental results, shown in Figure 2.6(b), where $\mu = 10^2$ was used for the MMSE estimates.[8] Clearly, the results from MMSE method show both higher resolution and a lower amplitude at the grating lobe, even though model errors to some degree degraded the MMSE reconstructions.[9]

The fact the MMSE estimates become more similar to DAS beamformed data for large values of μ, can be explained by the fact that the MMSE estimator reduces to a matched filter, $\mathbf{P}^T/\mu$, when μ is large. Since the DAS beamformer is a kind of matched filter as well, their performance will be similar. Thus, if the variance of the measurement noise is very high, then the MMSE estimator will reduce to a matched filter, which is known to maximize the local SNR.

From the results presented above it can be concluded that the MMSE estimator is capable of eliminating most of the grating lobe effects, if the SNR is sufficient. We will continue to investigate these properties of the MMSE estimator in the experiment presented below.

Experiment 2: Illustration of Grating Lobe Suppression for Parallel Array Imaging

In the second experiment the parallel DAS beamformer [1] and the MMSE estimator (2.14) were used to reconstruct a full image from a single emission from a wire target at a fixed position. More precisely, the entire 50 mm wide ROI was reconstructed from one emission.[10] Again, a 16-aperture of the 64 element 1D array, focused at z=50 mm and steered -20° in transmission, was used.

The profile plots of the reconstruction performance for two target positions was examined; the first one with the target in the main lobe at $x = -18$ mm, shown in Figure 2.7, and the second with the target located in the grating lobe at $x = 10$ mm, shown in Figure 2.8. The noise variance was constant in the simulations, which resulted in an SNR of 12.5 dB when the target was in the main lobe and a SNR of 10.7 dB for target in the grating lobe, according to the SNR is definition in (2.15).

Clear case of leakage from the main to the grating loge can be seen in Figure 2.7 showing the profiles for the target placed in the main lobe – the DAS beamformed data has a well pronounced peak at the grating lobe position, around $x = 10$ mm, for both the simulated and the measured data. This peak has been removed in the MMSE processed images, presented in Figures 2.7(b) and (d). The ability of the MMSE to reduce the leakage is even better demonstrated in Figure 2.8

---

[8] $\mu = 10^2$ resulted in the best visible performance.

[9] The synchronization in the ALLIN system is sometimes inexact which introduces modelling errors.

[10] Due to the limitations of the ALLIN system the "single" emission was emulated as in Experiment 1 above.

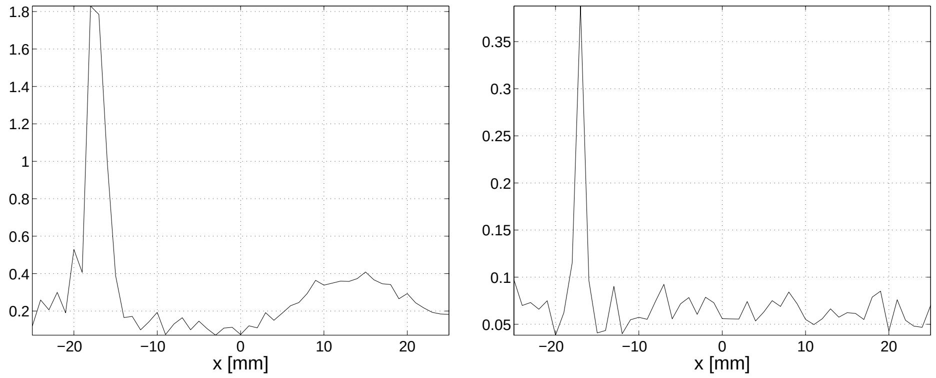

(a) Parallel DAS: Simulated data (SNR = 12.5 dB).

(b) MMSE: Simulated data (SNR = 12.5 dB).

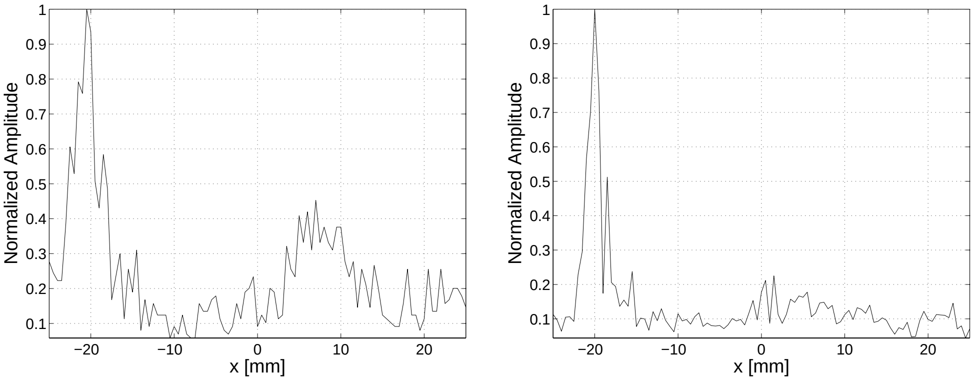

(c) Parallel DAS: Measured data.

(d) MMSE: Measured data.

Figure 2.7: Profile plots for parallel beamformed data with a point target in the main lobe using a 16 element 1D array focused at $z = 50$ mm and steered -20°.

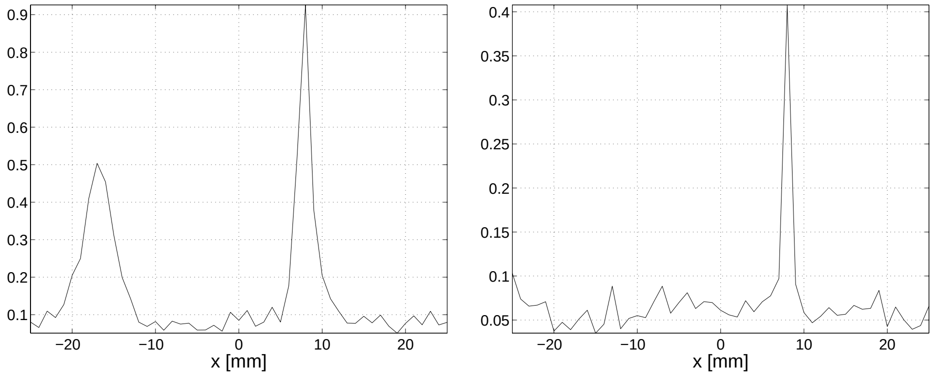

(a) Parallel DAS: Simulated data (SNR = 10.7 dB).

(b) MMSE: Simulated data (SNR = 10.7 dB).

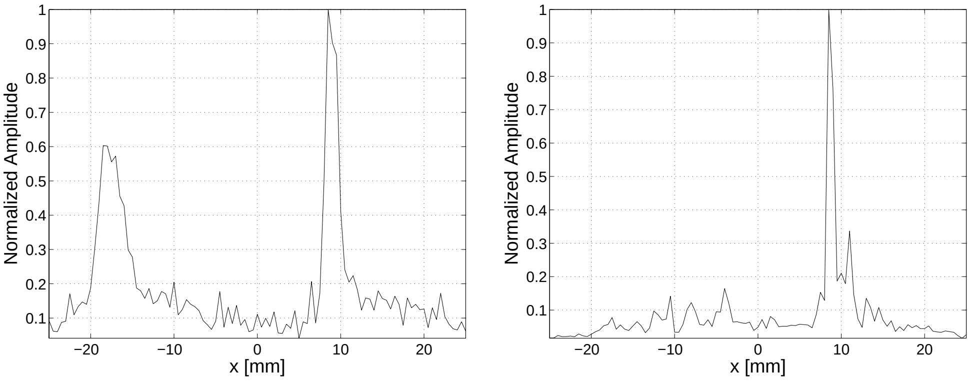

(c) Parallel DAS: Measured data.

(d) MMSE: Measured data.

Figure 2.8: Profile plots for parallel beamformed images with a point target in the grating lobe using a 16 element 1D array focused at $z = 50$ mm and steered -20°.

where the target is in the grating lobe. Then, the parallel DAS processed data shows clear leakage effect – strong peaks at both the main lobe and the grating lobe positions, even though there is only one target located in the grating lobe.

Also here the lateral resolution is superior for the MMSE method compared to the parallel DAS beamformer, and the width of the target peak in the MMSE reconstructed image is roughly half the width of the corresponding DAS image.

Thus, it can be concluded that the MMSE method has a very valuable feature – it can successfully compensate for grating lobes resulting from the use of under-sampled arrays. Essentially, the parallel MMSE beamformer can reconstruct a target regardless if it is located is in the main or in the grating lobe. The performance depends mainly on the acoustic energy at the particular target position.

2.5 Parallel Imaging with Exponential Priors

So far it has been assumed that each image element in the vector $\mathbf{o}$ could take both negative and positive values. Such an assumption is reasonable if the inspected object may have an acoustic impedance that can be both higher and lower from that of the surrounding medium. In some applications it may however be appropriate to assume that the scattering strength only can take positive values. Consider, for example, an experiment similar to the those discussed in Section 2.4.2 above where it is known *a priori* that the targets (e.g., wire) have a much higher acoustic impedance than the surrounding medium. Thus, the resulting scattering amplitude must be positive. By using this information, the reconstruction performance should be improved, especially for band limited systems where linear deconvolution typically leads to ringings [8].

A drawback of imposing the positivity restriction on the scattering amplitude is that a closed form expression for a MAP estimator can no longer be found. This can be a serious drawback in the imaging applications of ultrasonic arrays where the dimensionality is usually high. However, in some cases the MAP solution has a structure that enables the use of very efficient numerical methods. One such example is when the measurement noise is Gaussian and the prior distribution for $\mathbf{o}$ is the exponential PDF.[11]

The MAP estimate for an exponential prior and Gaussian measurement noise can be found by solving the optimization problem

$$\begin{aligned} \hat{\mathbf{o}} = \arg\min_{\mathbf{o}} \; & \frac{1}{2}(\mathbf{y}-\mathbf{P}\mathbf{o})^T\mathbf{C}_{\mathrm{e}}{}^{-1}(\mathbf{y}-\mathbf{P}\mathbf{o}) + \lambda_{\mathrm{o}}\mathbf{1}^T\mathbf{o} \\ \text{subject to} \quad & o_i \geq 0 \; \forall i. \end{aligned} \tag{2.17}$$

Eq. (2.17) is a quadratic programming (QP) problem with inequality constraints. QP problems have the important property that they always can be solved in a finite number of iterations, if a solution exists at all [9]. Here, the QP problem is convex since the Hessian matrix, $\mathbf{P}^T\mathbf{C}_{\mathrm{e}}^{-1}\mathbf{P}$ is positive semidefinite, which further facilitates the solution of the problem.

The estimate obtained by solving (2.17) will hereafter be denoted the *positivity constrained quadratic programming*, or PCQP, estimate. In the two experiments described below the PCQP estimate has been compared with the DAS beamformer, the matched filter (MF), and the linear MMSE estimator. The image to estimate consisted of about 5000 unknowns and all computations were performed, on as-of-today, standard PC hardware in less than an hour.

Below, the performance of the PCQP estimator is illustrated, using both simulated data and experimental data acquired using the Imasonic array.

---

[11] The exponential PDF defined as $f(t) = 1/\lambda e^{-t/\lambda}$ has mean λ and variance λ^2. This PDF is also reasonable in the sense that it is the maximum entropy distribution if the mean is known.

Experiment 1: Focused Array using Simulated Data

In this experiment the PCQP estimate was compared with the parallel DAS beamformer, the MMSE estimator, (2.14), and the matched filter, $\mathbf{K}_{\mathrm{MF}} = \mathbf{P}^T$. An 16-element aperture mm of the Imasonic array focused at $z = 50$ was simulated. The noise $\mathbf{e}$ was white with Gaussian amplitude distribution. A snapshot of the acoustic field around the focal point for this setup is shown in Figure 2.9. Since the array is under-sampled two grating lobes can be seen at approximately $x = \pm 23$ mm but most of the acoustic energy is focused in the main lobe in the vicinity of the center axis $x = 0$.

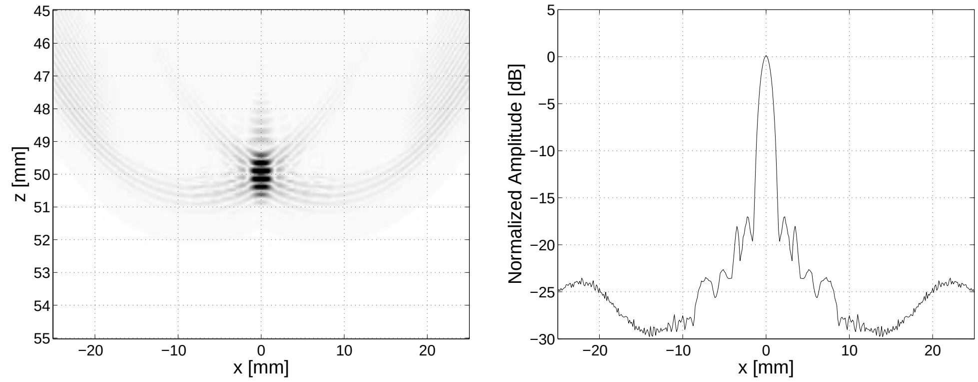

(a) Wave field snapshot at t = 37.3 μs. **(b)** Profile plot of the wave field.

Figure 2.9: Snapshot of the acoustic field at -25 mm $< x <$ 25 mm, 45 mm $< z <$ 55 mm for a 16-element aperture of the Imasonic array focused at z = 50 mm.

Three simulations were performed, with SNR = 30, 10, and -20 dB, were the SNR is defined by (2.15). The true scattering image, $\mathbf{o}$, had five pairs of unit area point targets located at the horizontal positions x=-25, -13, 0, 13, and 25 mm, and vertically at $z = 50$ and $z = 50.5$ mm, respectively. The vertical distance between the point targets is then roughly one wavelength corresponding to the center frequency of the array.

To obtain a fair comparison we need to set the parameters in the MMSE and the PCQP so that the expected energy using both estimators is the same. The prior that is determined by the mean value, λ_{o}, used in the PCQP estimator 2.17 was based on the assumption that a single unit area point target is expected in the ROI. The mean scattered energy over the ROI of the size MN is the sum of the squared mean value λ_{o} and the variance λ_{o}^2, which for a single point target becomes $1^2/MN = \lambda_{\mathrm{o}}^2 + \lambda_{\mathrm{o}}^2$. Thus, λ_{o} is given by $1/\sqrt{2MN}$. By a similar reasoning the variance, σ_{o}^2, used in the linear MMSE estimator is given by $\sigma_{\mathrm{o}}^2 = 1/MN$.

The reconstruction results, for the respective SNRs, are displayed in Figures 2.10, 2.11, and 2.12. Comparison of the images obtained using DAS and matched filter (MF) for the data with the relatively high SNR of 30 dB, presented in Figure 2.10, shows that those methods could only resolve the targets located close to the focal point. On the contrary, the MMSE and PCQP estimators were able to resolve all targets. The PCQP estimator had, as it can be seen in 2.10(f), very low error in the scattering amplitudes at all target positions. The MMSE estimator underestimated the amplitudes somewhat in the regions where the acoustic power was low[12], which is a reasonable behavior since due to the shape of transducer's beampattern the SNR in those regions is lower than at the focusing region and the estimates are therefore more uncertain.

---

[12] The true target amplitude was 1 in all cases.

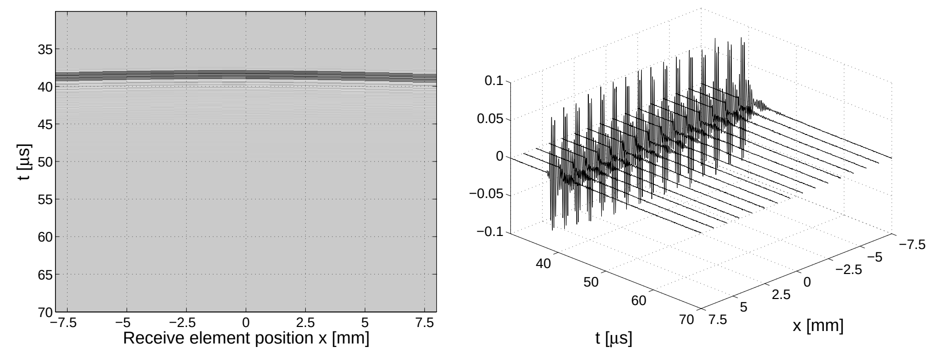

(a) Simulated data (B-mode image). **(b)** Simulated data.

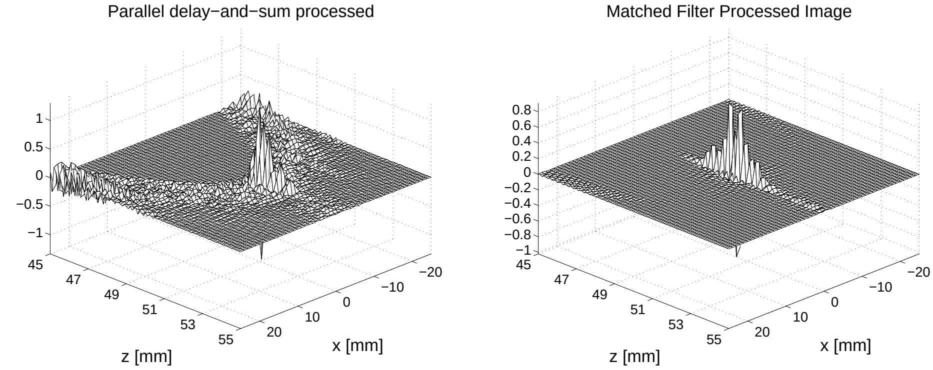

(c) DAS. **(d)** Matched filter processed image.

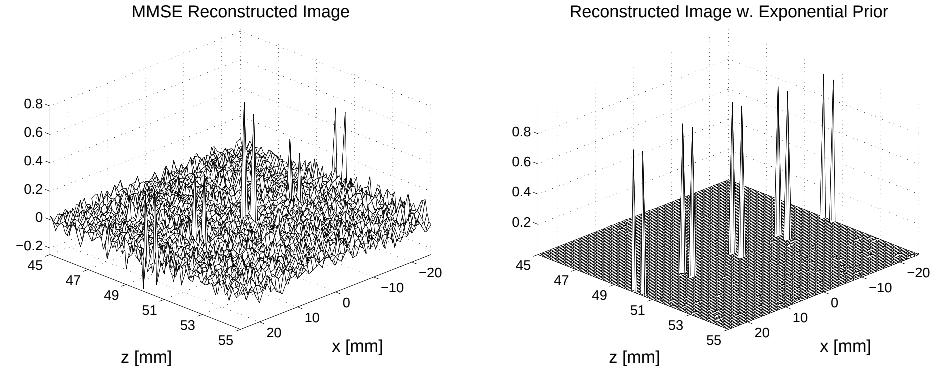

(e) MMSE. **(f)** PCQP.

Figure 2.10: Reconstructions using the DAS, MF, MMSE, and PCQP algorithms of simulated data corresponding to five pairs of point targets located at x=-25, -13,0 13, and 25 mm, at $z = 50$ and $z = 50.5$ mm, respectively.SNR equal to 30 dB.

When decreasing the SNR to 10 dB the PCQP estimate, shown in Figure 2.11, starts to show a similar behavior as the MMSE estimator, that is, it becomes more "cautious" at regions with lower acoustic power. This is even more evident in the reconstructions from the data with rather low SNR of -20 dB shown in Figure 2.12. Now, both the MMSE and PCQP estimators only "trust" responses from the focusing region and all other responses are close to zero. It is also noticeable that the MMSE reconstruction becomes more similar to the MF output as the SNR decreases, see Figures 2.12(d) and (e). This is due to the fact, mentioned above, that the noise covariance matrix, $\mathbf{C}_{\mathrm{e}}$, dominates the factor $(\mathbf{P}\mathbf{C}_{\mathrm{o}}\mathbf{P}^T + \mathbf{C}_{\mathrm{e}})^{-1}$ in the MMSE estimator when the SNR is low and the MMSE filter is then approximately $\mathbf{K}_{\mathrm{MMSE}} \approx \sigma_{\mathrm{o}}^2 \mathbf{P}^T (\sigma_{\mathrm{e}}^2 \mathbf{I})^{-1} = \mathbf{P}^T \sigma_{\mathrm{o}}^2 / \sigma_{\mathrm{e}}^2$.[13]

Figure 2.12(f) illustrates the remarkable high ability of the PCQP estimator to suppress the measurement noise. Even though the received signals were completely hidden in the noise, see Figures 2.12(a) and (b), the PCQP estimator managed to predict the two targets at the focal point with a noticeable high contrast in the reconstructed image.

It is evident from these simulations that the two model based methods, the MMSE and the PCQP, are superior to traditional DAS based beamforming, in the sense that DAS processing does not perform well for targets outside the focusing region, whereas the two model based methods can reconstruct the targets with high temporal and lateral resolution, provided that the SNR is sufficiently high.

Noticeable is also that, in contrast to the DAS and the MF beamformers, the overall amplitudes of the estimates become lower for both the MMSE and the PCQP estimators as the noise variance increases. In essence, the data becomes less informative regarding the scattering amplitudes in $\mathbf{o}$, when the noise variance increases, and therefore, the MMSE and PCQP estimators become more cautious and tend to underestimate the amplitudes.[14] This is a reasonable behavior which can serve as a warning that the quality of the data may be insufficient for our particular purpose.

The general observation from the above simulations is that the spatial distribution of acoustic energy that is more important for the reconstruction performance then the shape of the ultrasonic pulse. More specifically, the reconstruction performance of the model based methods employed here mostly depends on the SNR in the particular region[15] and not on the length or shape of the acoustic waveform. Moreover, as demonstrated above, the MMSE and PCQP estimators could estimate targets outside the focusing region, where the transmitted waveforms from each element are out phase, provided that the SNR was sufficient.

Experiment 2: Steered Array using Measured Data from Wire Targets

To verify the above mentioned conclusions, based on simulated results regarding the ability of the Bayesian estimators to reconstruct targets outside the main beam, an experiment with an under-sampled steered array is presented here. As was mentioned earlier, such an array will transmit energy both in the focusing direction and in the directions of the grating lobes. A relevant question is, therefore, if the Bayesian methods also are able to accurately estimate the scattering strength from a target located in a grating lobe?[16]

For this purpose, the parallel DAS, MMSE and the PCQP methods were used to reconstruct

---

[13] The gain of the MMSE estimator is lower than that of the MF due to the factor $\sigma_{\mathrm{o}}^2/\sigma_{\mathrm{e}}^2$, which will be low if the noise variance is high.

[14] The amplitudes go towards the *a priori* mean value, which was 0 for the MMSE estimates and $1/\sqrt{2MN}$ for the PCQP estimates in this case.

[15] The bandwidth of the ultrasonic system is also of importance [8].

[16] It should be noted that due to the effect of leakage to the main lobe resulting in ghost images the energy contained in grating lobes has never been used for imaging. The classical way of avoiding ghost images is eliminating grating lobes by proper array design.

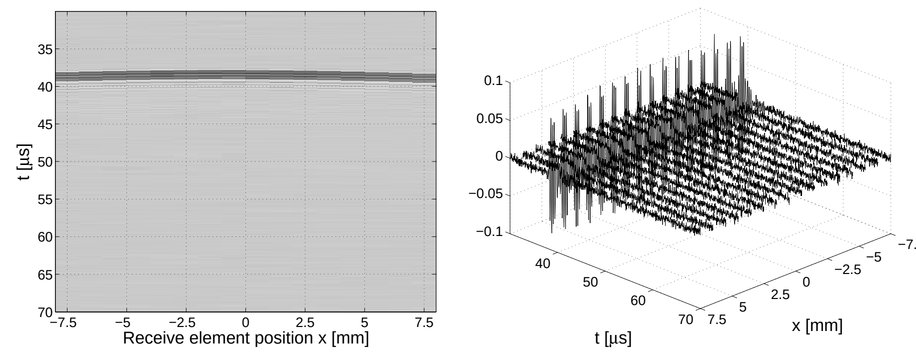

(a) Simulated data (B-mode image). **(b)** Simulated data.

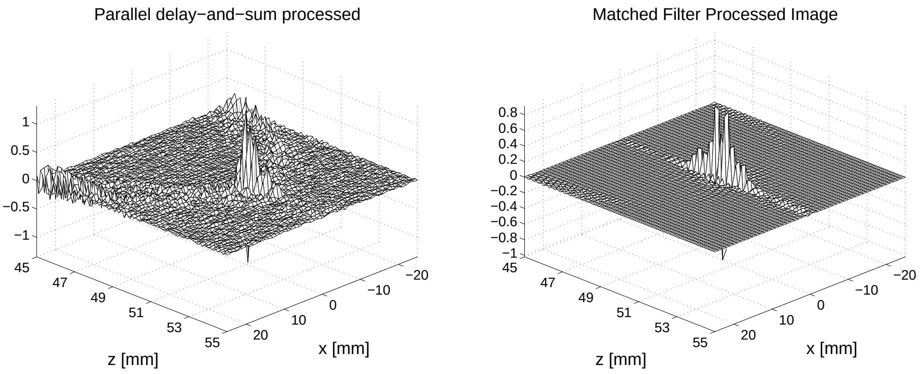

(c) DAS. **(d)** Matched filter processed image.

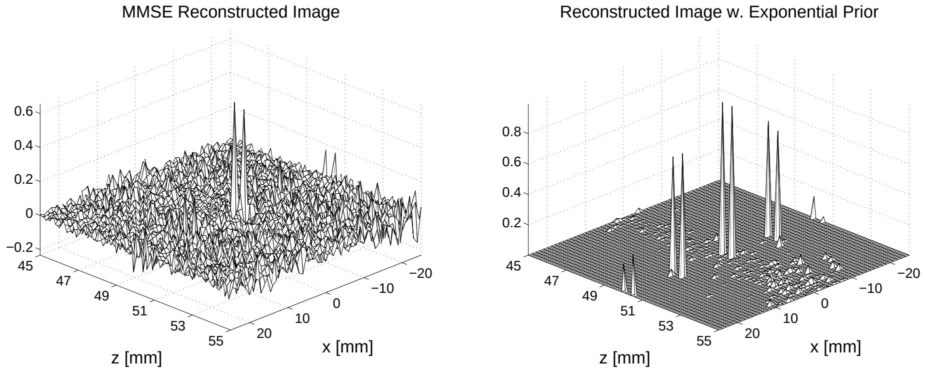

(e) MMSE. **(f)** PCQP.

Figure 2.11: Reconstructions using the DAS, MF, MMSE, and PCQP algorithms of simulated data corresponding to five pairs of point targets located at x=-25, -13,0 13, and 25 mm, at $z = 50$ and $z = 50.5$ mm, respectively. SNR equal to 10 dB.

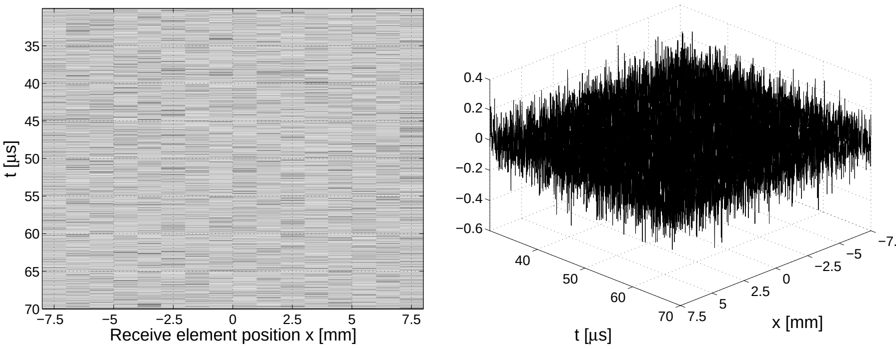

(a) Simulated data (B-mode image). (b) Simulated data.

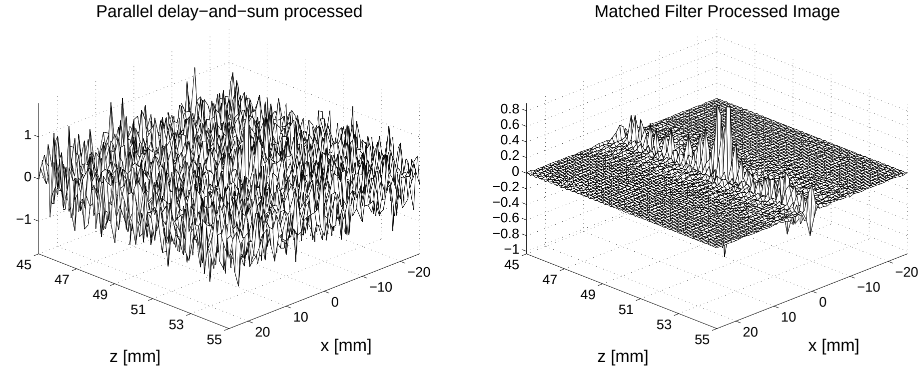

(c) DAS. (d) Matched filter processed image.

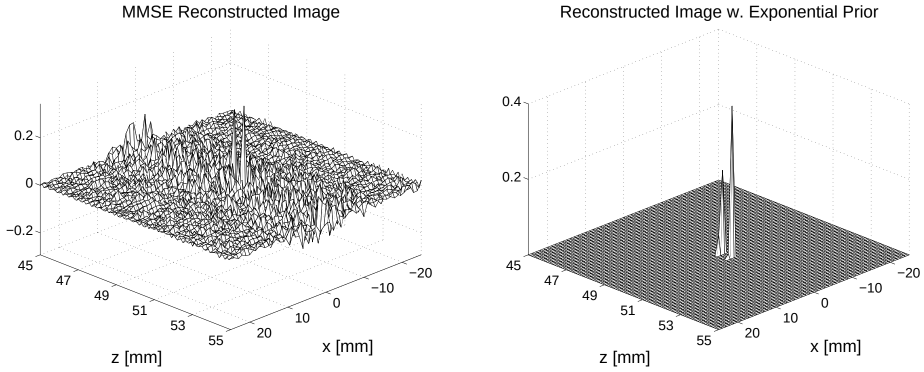

(e) MMSE. (f) PCQP.

Figure 2.12: Reconstructions using the DAS, MF, MMSE, and PCQP algorithms of simulated data corresponding to five pairs of point targets located at x=-25, -13,0 13, and 25 mm, at $z = 50$ and $z = 50.5$ mm, respectively. SNR equal to -20 dB.

data from a 16 element aperture the 64-element Imasonic array, focused at $z = 50$ and steered at -20°, acquired using the ALLIN system. A snapshot of the resulting wave field from this setup is presented in Figure 2.5 above. The measurements were performed using wire targets, positioned both in the main lobe at $x = -18$ mm and in the grating lobe at $x = 10$ mm, at depth $z = 50$ mm, see the illustration in Figure 2.13. The reconstruction results are shown in Figure 2.14.

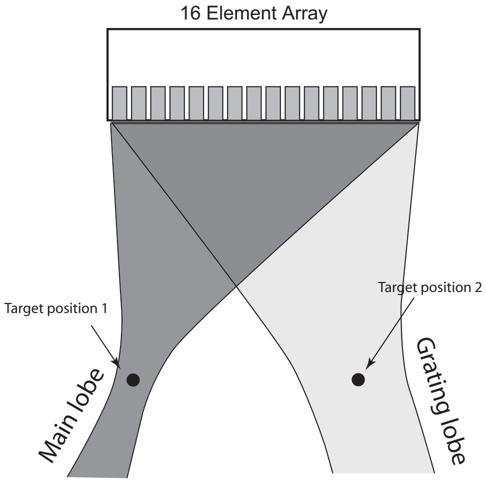

Figure 2.13: Illustration of the measurement setup for Experiment 2. The under-sampled 16 element aperture was focused at $z = 50$ mm and steered -20°. A snapshot of the wave field obtained for this configuration is presented in Figure 2.5.

The results obtained with the DAS method, shown in Figures 2.14(a) and (b), clearly demonstrate the typical leakage effect from the grating lobe associated with conventional beamforming. The temporal resolution for the DAS method is roughly the same as the length of the acoustic pulse for the target in the main lobe.[17] Also, the temporal resolution for the target in the grating lobe is very poor which can be explained by the fact that the acoustic waveform is much longer in the grating lobe than that at the focal point (cf Figure 2.5(a)).

As can be seen in Figures 2.14 (c)–(f), both the MMSE and the exponential MAP estimators suppressed the grating lobe well for both target positions, and the temporal resolution has also been improved compared to DAS processing. The MMSE estimates in Figure 2.14(d) have some ringings. This ringing behavior is most likely due to model errors caused by synchronization problems in the ALLIN array system. The PCQP estimates, shown in Figures 2.14(f) and (f), also have some extra "spikes" but the amplitude of those spikes are smaller than the oscillations in the MMSE estimates.

Evidently, both of the model based MMSE and PCQP estimators were able to accurately estimate the target strength both for the wire target located in the main and in the grating lobe. This is in complete agreement with the simulations in Experiment 1 above.

2.5.1 Concluding remarks

The results from the two experiments presented in this section (2.4) show that, at least for high contrast targets, the use of an exponential prior PDF for the scattering amplitudes can give impressive results with very high temporal and lateral resolution. The contrast in the recon-

---

[17] This is expected since in the standard DAS processing there is no compensation for the transmitted pulse waveform.

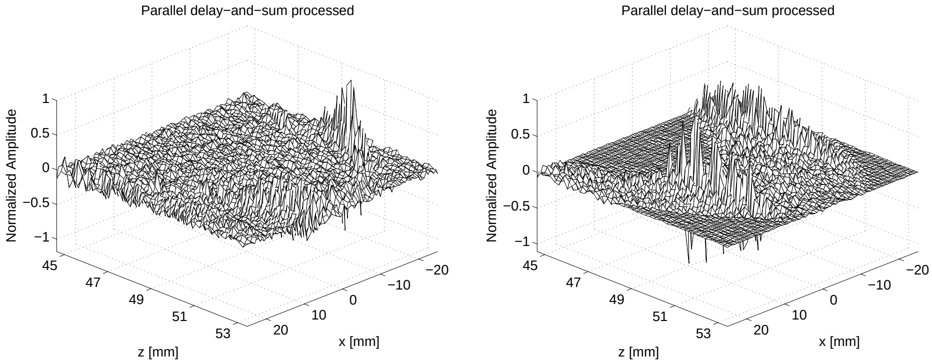

(a) DAS: Target in main lobe. **(b)** DAS: Target in grating lobe.

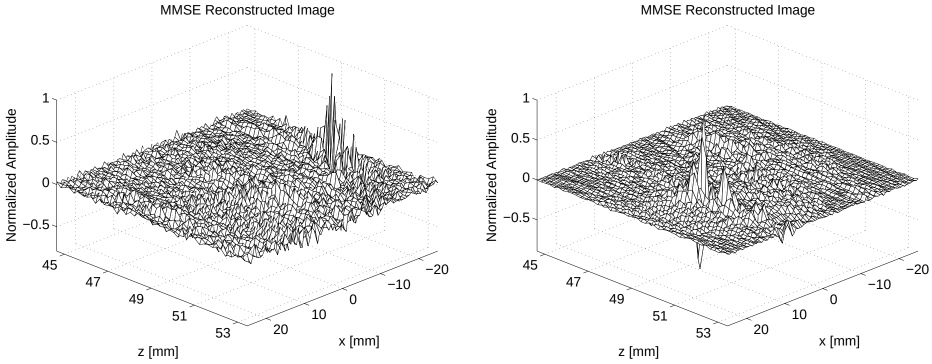

(c) MMSE: Target in main lobe. **(d)** MMSE: Target in grating lobe.

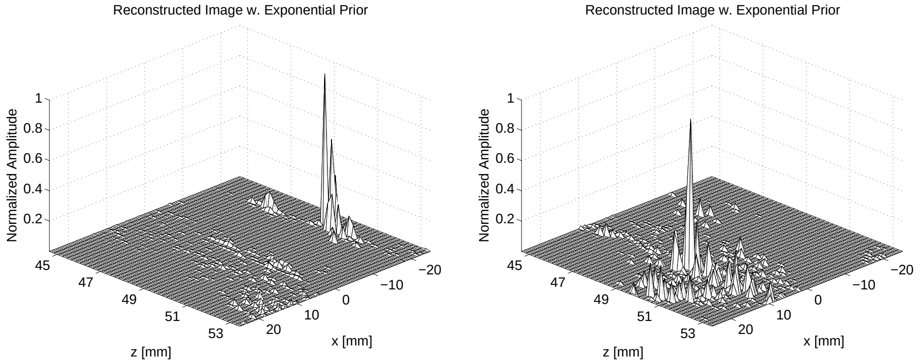

(e) PCQP: Target in main lobe. **(f)** PCQP: Target in grating lobe.

Figure 2.14: Reconstructions from measured data using a wire target in the main lobe (Figs. (a), (c), and (e)) and a wire target in the grating lobe (Figs. (b), (d), and (f)). The data were acquired using the ALLIN system and the 64-element concave Imasonic array. The transmitted beam was steered at -20 and focused at 50 mm using 16 array elements.

structions is also very high and the noise level is often very low. The remarkable performance of the exponential MAP estimator is due to the correct prior information that was incorporated into the model, which enables the estimator to effectively discriminate between noise and the target responses.

The most significant drawback of the PCQP method is that the estimate must be obtain by an iterative optimization algorithm. This makes the method most suitable for offline processing where real-time constraints are of little concern.

The transmit focusing delays in ultrasonic array imaging systems are often subject to quantization errors. This may result in a slightly different transmit beampattern from the desired one. In classical beamforming this will result in an increased sidelobe amplitudes [10, 11]. However, the model based estimators discussed here can compensate for these errors given that the true focusing delays are known.

In the experiments discussed in this chapter it was assumed that the scattering amplitudes at all image points were uncorrelated. In some applications the scattering objects can, for example, have a layered structure (e.g., in seismic exploration) resulting in correlations between the scatterers. This knowledge can be easily introduced in the linear MMSE estimator by means of the covariance matrix $\mathbf{C}_o$.

In the experiments performed with the ALLIN system presented in this chapter the *a priori* mean and variance of the scattering strength were in reality unknown. Despite this fact, the results obtained from both the linear MMSE and the non-linear PCQP methods showed that the exact values of mean or variance were not required. Our experience is that the reconstruction results for both these model based methods are not sensitive to the particular value of the variance or the mean. The variance or mean can typically be changed by a factor of 10 without significantly affect the reconstruction performance. Furthermore, it is possible to design an experiment, with a known set of scatterers, to estimate the unknown quantities. However, this is a topic for future research.

2.6 Summary

In this chapter we have evaluated performance of the linear MMSE estimator and the PCQP estimator used for the reconstruction of ultrasonic data in monostatic configuration as well as in multistatic parallel array imaging.

It was demonstrated that both estimators were capable of reconstructing multiple targets with high accuracy in the experiments even if the ultrasonic data were sparsely sampled. However, the PCQP estimator was more immune to the corrupting noise.

The MMSE estimator, which in the simplest case results in a spatio-temporal filter with only one scalar tuning parameter, clearly outperformed traditionally used DAS beamforming algorithms in terms of higher resolution for the targets immersed in water. In the parallel receive imaging, the MMSE algorithm clearly minimized target leakage from the grating lobes and could be successfully used for correct reconstruction of targets located in the grating lobes.

However, when more precise prior information on the scattering strength is available even better performance can be achieved using the nonlinear PCQP estimator developed for the exponential prior. This estimator clearly outperformed the linear MMSE estimators in terms of high immunity to the measurement noise and its ability to reconstruct multiple targets in the ROI.

The performance of the proposed estimators is achieved at the price of the increased computational complexity, especially, for the PCQP algorithm which takes the form of an iterative optimization algorithm.

Bibliography

[1] T. Stepinski, E. Wennerström, F. Lingvall, and P. Wu. Inspection of copper canisters for spent nuclear fuel by means of ultrasound — NDE of friction stir welds, nonlinear acoustics, ultrasonic imaging. Technical Report TR-04-03, SKB, 2003.

[2] F. Lingvall. *Time domain reconstruction methods for ultrasonic array imaging.* PhD thesis, Uppsala University, Signals and Systems, 2004.

[3] B. Piwakowski and K. Sbai. A new approach to calculate the field radiated from arbitrarily structured transducer arrays. *IEEE Trans. on Ultrasonics, Ferroelectrics, and Frequency Control*, pages 422–440, 1999.

[4] B. Delannoy, R. Toutguet, C. Bruneel, E. Bridoux, J.M. Rouvaen, and H. Lasota. Acoustical image reconstruction in parallel-processing analog electronic systems. *Journal of Applied Physics*, 50(5):3153–3159, May 1979.

[5] D.P. Shattuck, M.D. Weinshenker, S.W. Smith, and O.T. von Ramm. Explososcan: a parallel processing technique for high speed ultrasound imaging with linear phased arrays. *J. Acoust. Soc. Am.*, 75(4):1273–1282, April 1984.

[6] O.T. von Ram, S.W. Smith, and H.G. Pavy Jr. High-speed ultrasound volumetric imaging system. II. Parallel processing and image display. *IEEE Trans. Ultrason. Ferroelectr. Freq. Control*, 38(2):109–15, March 1991.

[7] B. Delannoy, R. Toutguet, C. Bruneel, E. Bridoux, J.M. Rouvaen, and H. Lasota. Acoustical image recosntruction in parallel-processing analog electronic systems. *J. Appl. Phys.*, 50(5):3153–3159, May.

[8] T. Olofsson. *Maximum a posteriori Deconvolution of Ultrasonic Data with Applications in Nondestructive Testing: Multiple transducers and rubustness issues.* PhD thesis, Uppsala University, 2000.

[9] J. Nocetal and S.J. Wright. *Numerical Optimization.* Springer-Verlag, 1999.

[10] B.D. Steinberg. Digital beamforming in ultrasound. *IEEE Transactions on Ultrasonics, Ferroelectrics, and Frequency Control*, 39(6):716–721, November 1992.

[11] S. Holm. Analysis of worst-case phase quantization sidelobes in focused beamforming. *IEEE Transactions on Ultrasonics, Ferroelectrics, and Frequency Control*, 39(5):593–599, September 1992.

Chapter 3

Evaluation of Ultrasonic Attenuation in Copper

by Ping Wu and Tadeusz Stepinski

3.1 Introduction

Performance of an ultrasonic system used for the nondestructive evaluation (NDE) of welds in copper canisters is influenced by the grain structure and ultrasonic attenuation of copper material. In this chapter we present results of an evaluation of a number of copper samples in order to investigate the correlation between grain size, ultrasonic attenuation and defect detectability in copper material used for SKB's canisters.

Since ultrasonic attenuation is related to essential material parameters it has been widely used for materials characterization. Various measurement methods have been developed to evaluate ultrasonic attenuation. However, results obtained using most simple techniques do not yield true values since they produce results that depend on the measurement setup (particularly, on transducer's diffraction effects).

Two objective techniques that are established and recommended by the American Society for Testing and Materials (ASTM) as International standards E 664-93 and C 1332-01 [1, 2] are the immersion method (IM) and the buffer rod method (BRM). Both of them are single side methods, essentially based on the same theory, although the IM is performed in the immersion and the BRM in the air, which results in different reflection coefficients from the back surface of the specimen. Common advantage of these methods is that they can be implemented in pulse-echo mode, which means that only one side access to the inspected materials is required.

In the present work, only the IM is used to evaluate ultrasonic attenuation in copper blocks with different grain size. The use of BRM is proposed in a portable hand-held device aimed for the evaluation of attenuation of canister copper material at SKB's Canister Laboratory.

Generally, two main factors contribute to the ultrasonic attenuation in a solid material for wavelengths used in NDE: (i) scattering attenuation due to losses caused by multiple reflections from the internal material discontinuities, such as grain boundaries and inclusions, and (ii) absorption attenuation caused by thermoelastic loss, dislocation motion, and mechanical hysteresis [3–7]. The attenuation in copper for ultrasonic frequencies in the MHz range is determined almost entirely by scattering attenuation (since copper is a poly-crystalline metal consisting of collections of grains in different amounts and configurations, and the attenuation of a poly-crystalline metal in most cases is dominated by scattering attenuation [4, 5]). Therefore, ultrasonic attenuation is closely related with the microstructure of copper, e.g., grain size, grain shape, grain-size distribution. In other words, the copper material's microstructure directly influences its attenuation.

In the present research, the IM is used to evaluate the attenuation in a number of copper specimens with various grain size. Thirteen copper blocks coming from two different batches have been inspected in total. The first batch included ten copper blocks were prepared from the same parent material, nine of them were heat treated in series by the Swedish Institute for Metal Research (SIMR) who also delivered three specimens from the second batch.

The following issues are addressed in our research:

- Basic theory of attenuation measurements, focused on IM.
- Systematic error introduced by transducer's diffraction effect. Diffraction correction for planar transducers that can easily be applied to the attenuation evaluation has been implemented in MATLAB. The results obtained using planar transducers are compared with those obtained using focused transducers without diffraction correction.
- Comparison of the results obtained using two ultrasonic instruments RITEC and ALLIN. RITEC an Agilent Digital Scope was used as a reference.
- The influence of ultrasonic attenuation on the defect detectability is studied.

The following text is organized as follows: a short presentation of basic theory of the buffer-rod and the immersion methods is given in the beginning (the detailed derivation is provided in the appendix 3.A). Then the measurement setup and copper specimens are specified and the measurements made on copper specimens are presented. Finally, the obtained results are discussed and conclusions are made.

3.2 Methods for attenuation evaluation

Below, we present the buffer-rod method (BRM) and the immersion method (IM) that are often used for evaluating ultrasonic attenuation in solid materials. The methods are applicable to specimens with parallel front and back surfaces. In both methods, an intermediate material characterized by a low acoustic impedance (a solid buffer rod in BRM and water path in IM) is used between the ultrasonic transducer and the inspected specimen. Although the BRM and the IM are based on the same principle the difference in setups results in different formulas for calculating the attenuation. A detailed derivation of the theory is given in Appendix 3.A.

3.2.1 Buffer rod method

The buffer rod method (BRM) was proposed by E. P. Papadakis in 1968 [8, 9]. The basic theory applies to the reflection and transmission of a plane wave (or a non-diffracted beam) at the planar interfaces including buffer/sample interface and specimen's back surface. However, since finite-sized aperture transducers are used in practical attenuation measurements the planar wave assumption does not hold. Consequently, the diffraction (beam spreading) effect has to be taken into account since it may cause large evaluation error when the BRM is used to evaluate attenuation in thick specimens. The beam spreading effect results in an apparent attenuation that is superimposed on the true material attenuation. Moreover, since the diffraction effects of a finite-sized transducer depend on wavelength, the error due to the apparent attenuation is frequency dependent. For example, in our typical measurement performed on a copper block with a 60-mm thickness in the immersion test in water with a path length of 44 mm, the error due to the apparent attenuation can be as large as 40 dB/m for a 2.25-MHz transducer with a 10-mm diameter. Thus, when absolute measurements are performed for thick specimens the diffraction correction has to be introduced. The procedure of diffraction correction for attenuation measurements using the BRM was first specified in 1973 by Papadakis [10] and also presented in his later papers [11–13].

The BRM method can be applied for both narrow-band and broad-band transducer excitations provided that the diffraction correction can be computed for the setup used in the measurement in the respective frequency band. The corrections for planar circular transducers can be found in the literature, see e.g. [10]. The BRM method requires parallel front and back surfaces both for the buffer-rod and the specimen. Excessive roughness of the specimen's surfaces affects the measurements [14]. To facilitate understanding we present the BRM principle for a single frequency continuous wave excitation. However, the theory presented below can be easily extended to the broad-band case using Fourier transform and it can be implemented in modern digital ultrasonic instruments.

Assume that a transducer sends a continuous ultrasonic wave with an amplitude of I and a frequency of f towards a specimen through an intermediate medium (buffer) in a setup shown in Fig. 3.1. If the specimen and buffer have different acoustic impedances the wave will be reflected at the front and back interfaces of the specimen. Assume that the amplitude of the echo from the front interface is $A = A(f)$, and the amplitudes of the first and second echoes from the back interface are $B = B(f)$ and $C = C(f)$, respectively (Fig. 3.1). In the broad-

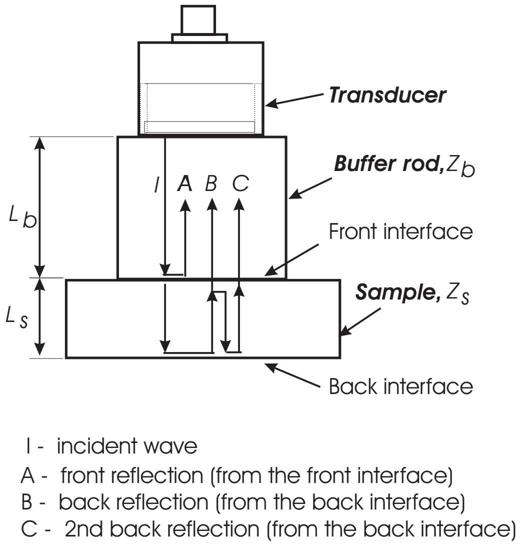

Figure 3.1: Setup used in buffer rod method. Back surface of the test specimen is in air.

band case, the amplitudes are found by taking the Fourier transforms of the respective echoes. The attenuation coefficient $\alpha = \alpha(f)$ of the sample with a length of L_s can be found from the measured amplitudes in the following manner (for details see [10])

$$\alpha = \frac{1}{2L_s} \ln\left(-R\tilde{B}\right) \tag{3.1}$$

where the reflection coefficient R for the interface between buffer and sample is determined by

$$R = \sqrt{\frac{\tilde{A}/\tilde{B}}{\tilde{A}/\tilde{B} - 1}} \tag{3.2}$$

and

$$\tilde{A} = \frac{A}{B} \tag{3.3}$$

$$\tilde{B} = \frac{B}{C} \tag{3.4}$$

α in Eq. (3.1) is in Nepers/m, and in terms of dB/m, it should be written as

$$\alpha = \frac{1}{2L_s} 20 \log_{10}\left(R\tilde{B}\right) \tag{3.5}$$

It is easy to find that 1 Neper = 8.6858 dB.

Eqs. (3.1) and (3.5) are valid provided that bottom reflection of the ultrasound wave in the test sample is complete, which is approximately valid in air.

3.2.2 Immersion method

In the immersion setup the sample is surrounded by water and the bottom reflection is not complete any longer.

In the immersion inspection, the attenuation coefficient is defined by the relation

$$\alpha = \frac{1}{2L_s} 20 \log_{10}\left(R^2\tilde{B}\right) \tag{3.6}$$

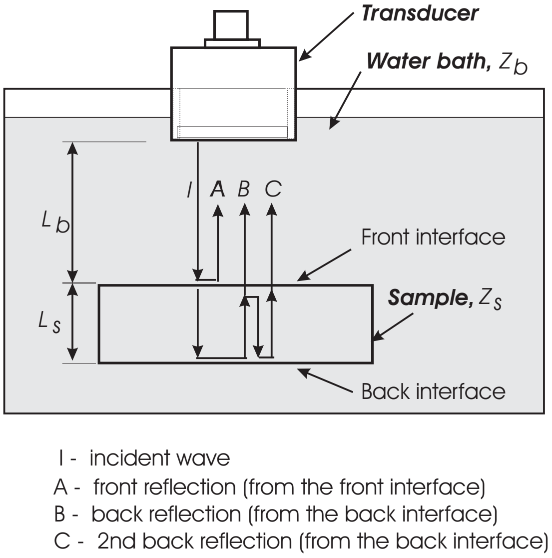

Figure 3.2: Immersion method. Back surface of the test specimen is in water.

which is different from that in the buffer rod method (Eq. (3.5))due to the difference in bottom reflection coefficient. Note that misusing Eq. (3.5) in the immersion method may lead to an error which depends on the difference in impedances between the sample and the immersing fluid. When the acoustic impedances of the sample and the immersing fluid differ very much, the error is not large, e.g., the acoustic impedance of the copper immersed in water is 27.57 times that of water so that $R = 0.93$, and $R^2 = 0.86$. Eq. (3.5) gives 0.6303 dB error. However, for samples with low acoustic impedances the error can be significantly large.

3.2.3 Diffraction correction

Diffraction correction is needed to compensate for diffraction loss (or beam spreading loss). Generally, diffraction loss (DL) results in an estimation error, which depends on the sample thickness. As it was already mentioned, DL may result in an "apparent attenuation" even if a material had no attenuation. Therefore, DL leads to the overestimated values of attenuation. Planar transducers and focused transducers of the same size have different beam patterns and the resulting diffraction correction for both types of transducers will be different. Calculating diffraction correction for a planar transducer is much easier than for the focused one. One DL curve that shown in Fig. 3.3 is plotted as a function of the normalized distance and, therefore, it can be applied to circular transducers with different radii and at different frequencies. In the present work the diffraction correction is only performed for planar circular transducers.

For broad-band excitation the diffraction correction has to be performed for each frequency in spectrums of the respective echoes, which means that the respective DL values need to be calculated first. Based on the angular spectrum approach proposed in our previous work [15, 16], we implemented the calculation of the DL (Fig. 3.3) in MATLAB. With this calculated DL curve, the diffraction correction can be introduced automatically into attenuation evaluation.

The automatic diffraction correction is performed in steps (for details see Appendix 3.A):

- find the DL values, DL_A, DL_B and DL_C, of the front echo A, the 1st back echo B and the 2nd back echo C on the curve in Fig. 3.3 at the following normalized distances of the corresponding echoes:

$$S_A = \frac{2L_b c_b}{a^2 f} \tag{3.7}$$

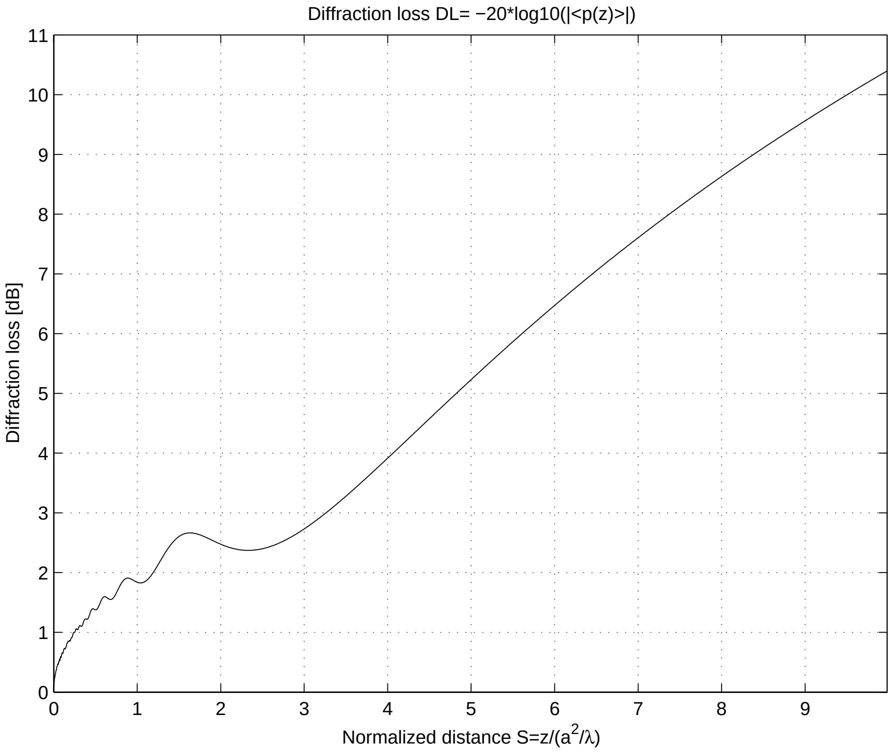

Figure 3.3: Diffraction loss in dB as a function of normalized distance $S = z/(a^2/\lambda)$. Note that the normalized distance S is frequency dependent.

$$S_B = S_A + \frac{2L_s c_s}{a^2 f} \tag{3.8}$$

$$S_C = S_A + \frac{4L_s c_s}{a^2 f} \tag{3.9}$$

where c_b and c_s are the sound speeds in the buffer and the sample, respectively;

- correct for the amplitudes of A, B and C in the following way

$$A_c = A \cdot 10^{DL_A/20} \tag{3.10}$$

$$B_c = B \cdot 10^{DL_B/20} \tag{3.11}$$

$$C_c = C \cdot 10^{DL_C/20} \tag{3.12}$$

- replace A_c, B_c and C_c for A, B and C in Eqs. (3.2), (3.5) and (3.6) to obtain to the corrected attenuation for the BRM setup

$$\tilde{\alpha} = \frac{1}{2L_s} 20 \log_{10} \left(R_c \tilde{B}_c \right) \tag{3.13}$$

and the corrected attenuation for the IM setup, respectively

$$\tilde{\alpha} = \frac{1}{2L_s} 20 \log_{10} \left(R_c^2 \tilde{B}_c \right) \tag{3.14}$$

where

$$R_c = \sqrt{\frac{\tilde{A}_c/\tilde{B}_c}{\tilde{A}_c/\tilde{B}_c - 1}} \tag{3.15}$$

$$\tilde{A}_c = \frac{A_c}{B_c} \tag{3.16}$$

$$\tilde{B}_c = \frac{B_c}{C_c} \tag{3.17}$$

3.3 Samples and Measurement Setup

3.3.1 Samples - copper blocks

Thirteen copper blocks provided by the Swedish Institute for Metal Research (SIMR) grain sizes and geometries specified in Fig. 3.4 were inspected. The first ten blocks with numbers 8420 to 8429, belong to the first batch; all of them have a 60-mm thickness and four flat bottom holes (FBHs) with diameters of 1, 2, 3 and 4 mm drilled in the bottom (Fig. 3.5). Optical microscopic graphs of those samples are shown in Fig. 3.6. It should be pointed out that bottom quality of the bottom drilled holes depends on their diameter, i.e., only the bottom-drilled holes of larger diameters (2, 3 and 4 mm) had relatively flat bottoms, while the quality of the 1-mm holes was lower. It was probably the reason that the ultrasonic scattering from the 1-mm holes was not strong enough to be visible in the ultrasonic images (C-scans) of most of the blocks from the first batch.

The other three blocks, referred to as Cu197, Cu214 and Cu282, with optical microscopic graphs are shown in Fig. 3.7 belong to the second batch without bottom holes.

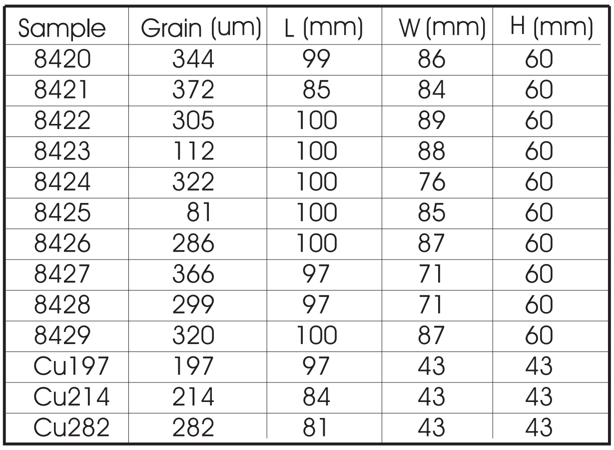

Sample	Grain (um)	L (mm)	W (mm)	H (mm)
8420	344	99	86	60
8421	372	85	84	60
8422	305	100	89	60
8423	112	100	88	60
8424	322	100	76	60
8425	81	100	85	60
8426	286	100	87	60
8427	366	97	71	60
8428	299	97	71	60
8429	320	100	87	60
Cu197	197	97	43	43
Cu214	214	84	43	43
Cu282	282	81	43	43

Figure 3.4: Geometry and grain size of the inspected specimens.

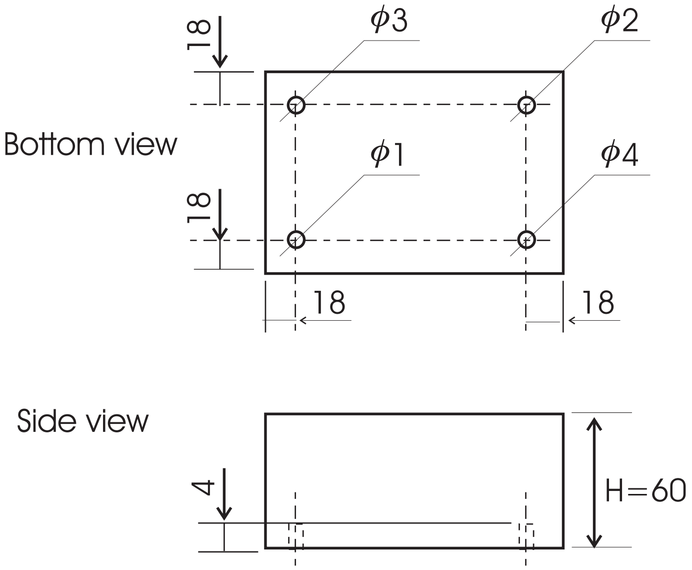

Figure 3.5: Geometry of the flat bottom holes in copper blocks.

3.3.2 Measurement setups

Two setups using different ultrasonic instruments were used to make measurements to evaluate attenuation of the copper blocks (Fig. 3.8). The first one, which was used as a reference consisted of the RITEC system (for sending and receiving ultrasonic signals) and the Infiniium 54810AR digital oscilloscope from Agilent Technologies (for recording the received ultrasonic signals). In the second setup the ALLIN system was used that can send, receive, and record ultrasonic signals.

Two different transducers were used in the measurements: (i) a focused transducer PANAMETRICS V307 with a nominal Frequency of 5 MHz, a diameter of 25 mm and focal distance 190 mm, and (ii) a planar transducer PANAMETRICS V325 with a nominal frequency of 2.25 MHz, and a diameter of 10 mm. The immersion method shown in Fig. 3.8 was used in all attenuation measurements.

The reason for using the focused transducer was difficulty with getting the second back surface echoes *C* (i.e., echo *C* Fig. 3.1) in all the copper blocks. Those echoes had a tendency to drown in noise when using the planar transducer for coarse grain blocks.

In the measurements made on all the blocks the front surface echo, the 1st back surface echo and the 2nd back surface echo needed in the evaluation of attenuation using Eq. (3.14) were recorded.

In addition to attenuation evaluation, the effects of attenuation on defect detectability of ultrasonic inspection were also investigated. For this purpose the first batch of ten blocks with FBHs were inspected using ALLIN system with the Panametrics focused transducer. The water path was approx. 25 mm which resulted in the focal depth of approx. 54 mm in copper.

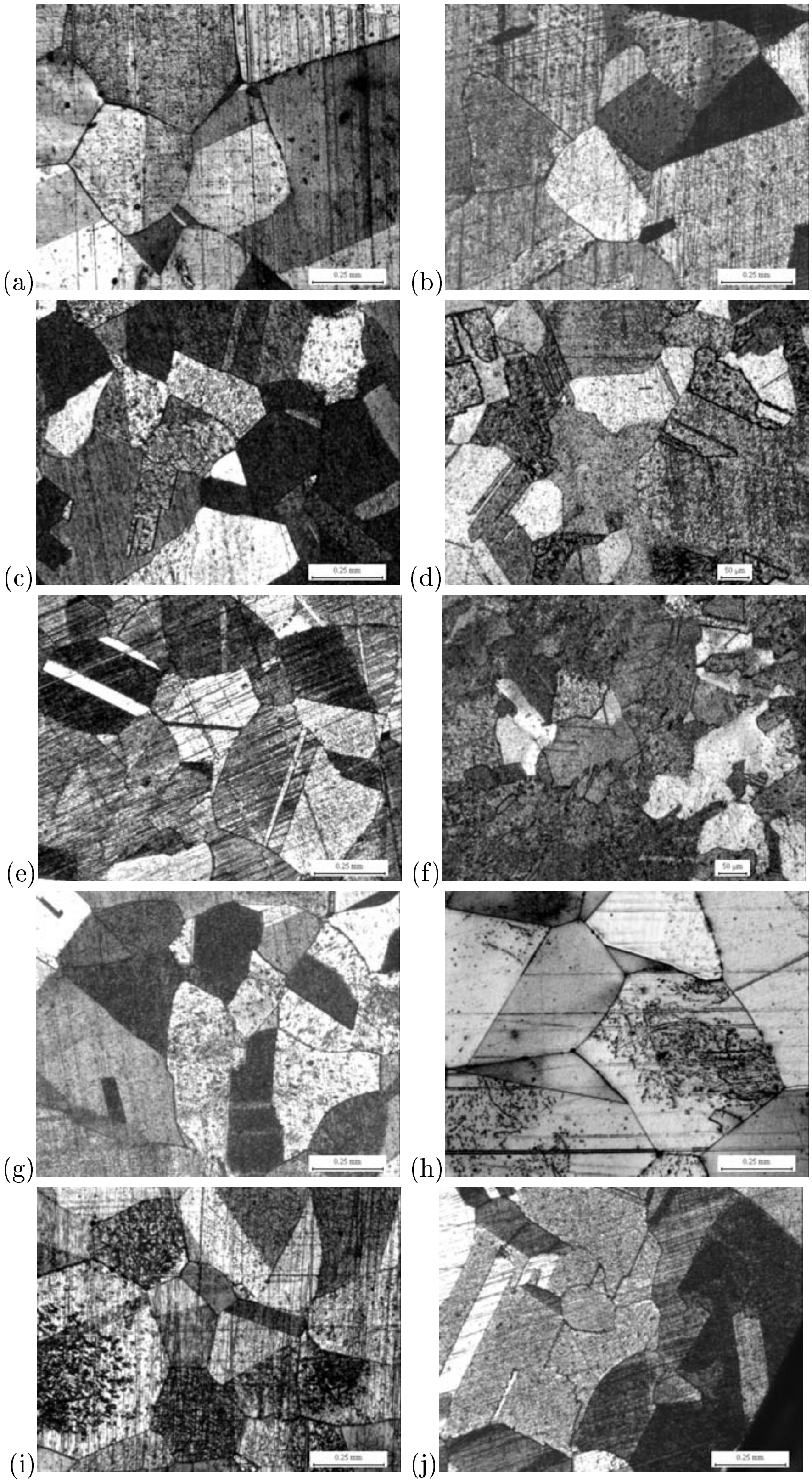

Figure 3.6: Optical microscopic graphs of the samples (a) Nr. 8420 (344 μm), (b) Nr. 8421 (372 μm), (c) Nr. 8422 (305 μm), (d) Nr. 8423 (112 μm), (e) Nr. 8424 (322 μm), (f) Nr. 8425 (81 μm), (g) Nr. 8426 (286 μm), (h) Nr. 8427 (366 μm), (i) Nr. 8428 (299 μm), (j) Nr. 8429 (320 μm).

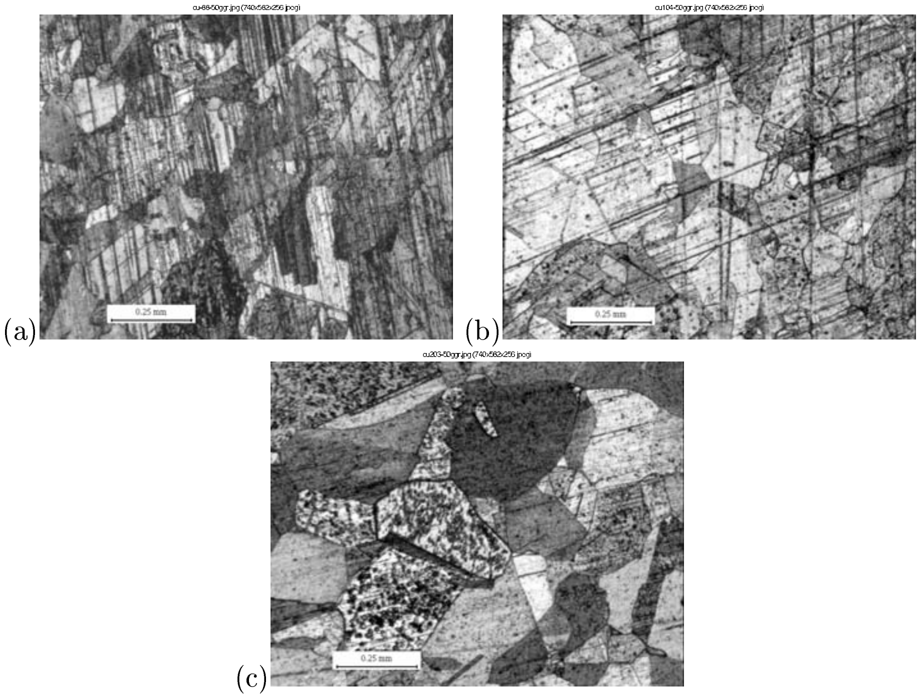

Figure 3.7: Optical microscopic graphs of the samples (a) Cu197 (197 μm), (b) Cu214 (214 μm), (c) Cu282 (282 μm).

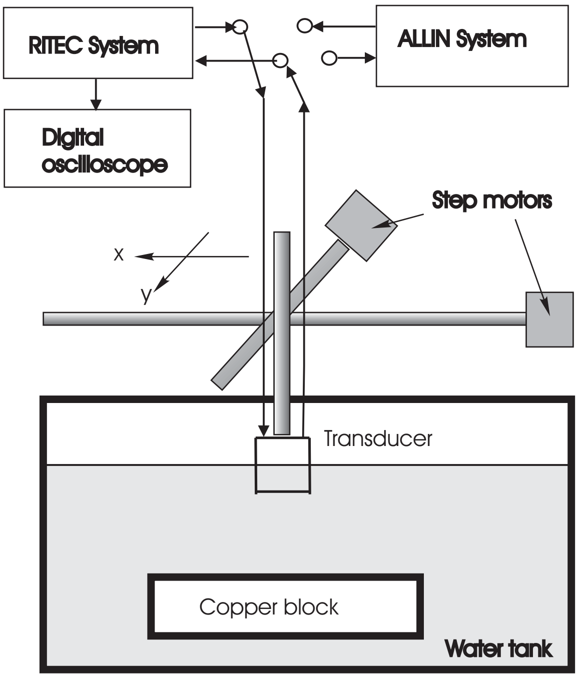

Figure 3.8: Measurement setup.

3.4 Results and discussions

3.4.1 Attenuation evaluation using RITEC system with 5 MHz focused transducer

The measurements presented in this section were made on all the 13 blocks using the RITEC system, the Agilent digital oscilloscope and the Panametrics 5 MHz focused transducer. The setups used for the batch 1 and 2 were slightly different due to the difference in block thickness and, therefore, the respective results are presented separately.

The water path for blocks from batch 1 (8420 – 8429) was 44 mm which resulted in the desired echo pattern where both back surface echoes (B and C) arrived before the second front echo (from water-copper interface). For blocks from batch 2 (Cu197, Cu214 and Cu282) the respective water path was approx. 84 mm. In both cases, the position of the focal zone inside the copper blocks was located nominally at a distance of approx. 12-15 mm from the back surface. It should be noted, however, that due to the finite aperture of the transducer actual focal zone was be shifted closer to the front surface. The attenuation coefficients were evaluated using Eqs. (3.2), (3.3), (3.4) and (3.6) (no diffraction correction was applied).

The results for 5 blocks selected from batch 1 are shown in Fig. 3.9 where it can be clearly seen that the attenuation is a nonlinear function of frequency. It should be noted, however, that only the monotonic parts of the attenuation curves in the lower frequency band are relevant. Since material attenuation increases rapidly with frequency, transducer energy in higher parts of its spectrum is insufficient for obtaining reliable attenuation estimates. This effect clearly depends on the specific material – the attenuation curve of 81 μm is monotonic in the whole frequency range 0.5 to 3.5 MHz presented in Fig. 3.9 while the 366 μm curve breaks at approx. 2.1 MHz. Generally, attenuation for the copper blocks tends to increase with material grain size with the exception of the 366 μm specimen which has the highest attenuation among the specimens presented in Fig. 3.9. This is not the only example of inconsistency for the specimens from the batch 1. Similar inconsistency can be observed in Fig. 3.10 showing bars corresponding to the attenuation coefficients of all 10 blocks from this batch measured at frequency 2 MHz. To facilitate analysis the attenuation of two fine-grain specimens, 81 and 112 μm, is presented separately in the upper part of Fig. 3.10. Note that the attenuation coefficients have been normalized by frequency and the result is in dB/m/MHz.[1]

From Fig. 3.10 it can be seen that the 286 μm specimen is a clear outlier with an extraordinarily large attenuation, other samples that are inconsistent with the trend are those with grain size 372 μm, 344 μm.

It should be pointed out that since ultrasonic attenuation is not a linear function of frequency, the attenuation estimated at a certain frequency f_0 is insufficient for estimating the attenuation at other frequencies $f \neq f_0$. Indeed, from Fig. 3.9 it can be seen that at 2.0 MHz, the attenuation of the ten blocks with the grains from 81 to 372 μm ranges from 30 to 180 dB/m, and at 2.25 MHz, the attenuation ranges from 39 to 221 dB/m.

Separate attenuation evaluation was made for blocks from the second batch (Cu197, Cu214 and Cu282). The results are presented in Fig. 3.11 showing the respective attenuation curves in the frequency range 0.5 to 5 MHz. Obtaining relevant values of attenuation in a broader frequency range than that for the specimens form the first batch using the same 5MHz transducer was possible thanks to the lower material thickness (43 mm in batch 2 instead of 60 mm in batch 1, cf Fig. 3.4). In Fig. 3.11 an inconsistency can also be seen, namely, the attenuation in the smaller grain block (197 μm) is even larger than those with 214 and 282 μm grains.

---

[1] This way of normalization is commonly used but it is justified only for media with linear attenuation in frequency.

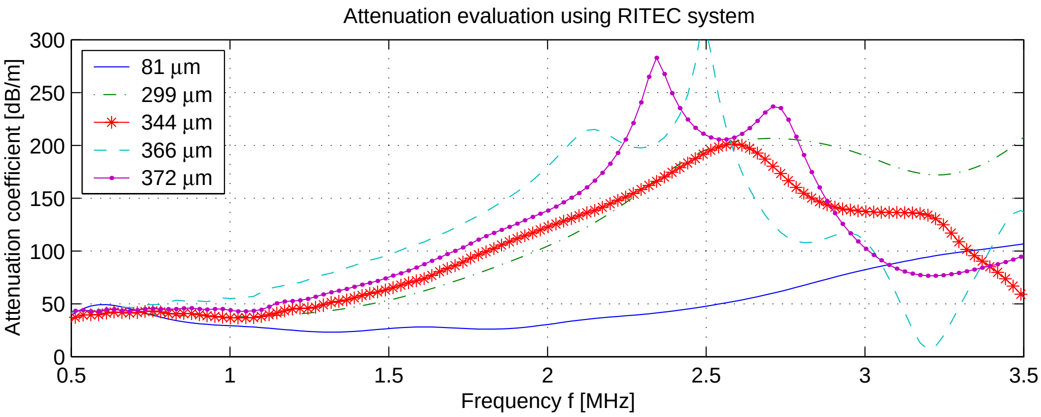

Figure 3.9: Attenuation evaluated using RITEC system and the 5MHz focused transducer as a function of frequency.

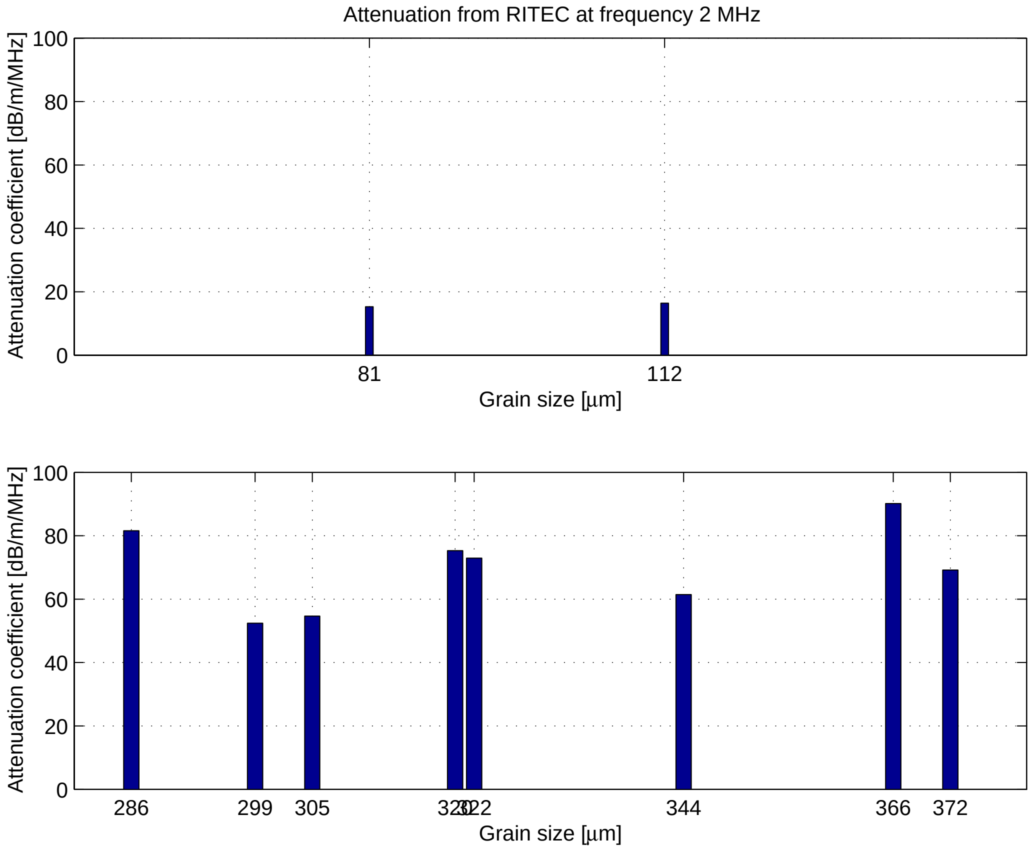

Figure 3.10: Attenuation coefficients [dB/m/MHz] at frequency 2 MHz. Note that α is normalized by frequency. In the upper panel are shown the attenuation coefficients of the fine grain specimens, and in the lower panel are the coefficients of the specimens with coarser grains ranging from 280 to 380 μm.

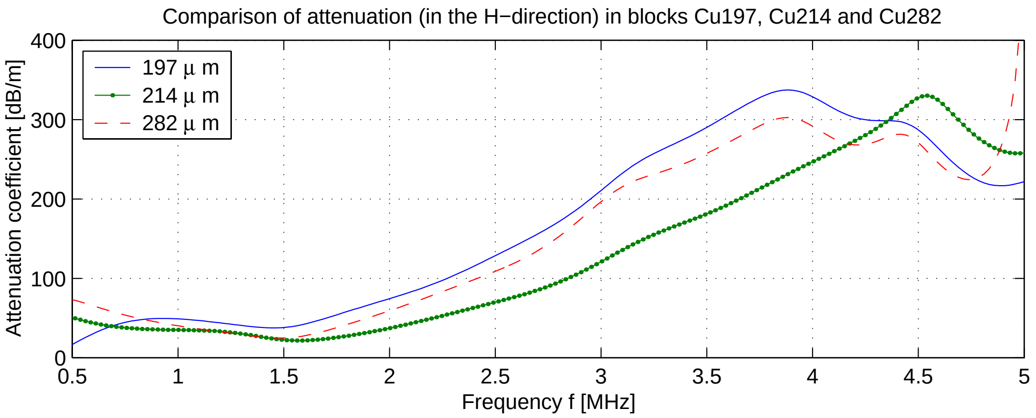

Figure 3.11: Attenuation coefficients in copper blocks from batch 2, evaluated using RITEC system and 5 MHz focused transducer.

3.4.2 Attenuation evaluation using ALLIN system with focused 5 MHz transducer

Attenuation in all blocks in batch 1 and 2 was also evaluated using the ALLIN system, in order to see how different the results from a different system would be. By switching the cable from RITEC system to ALLIN system (see Fig. 3.8), we made the measurements for identical immersion setups. This means that the transducer position on the specimen and the distance to the front surface were exactly the same for the two measurement systems. The results obtained using the ALLIN system with the 5 MHz focused transducer, as shown in Fig. 3.12, are in good agreement with those from the RITEC. However, the noise level in the signals from the RITEC system was smaller, and thus, the RITEC performed a little better, especially at high frequency range.

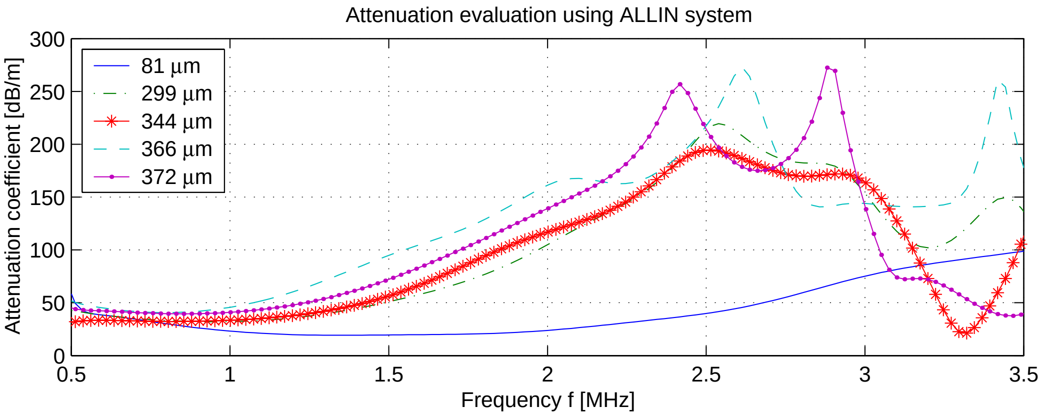

Figure 3.12: Attenuation evaluated using ALLIN system and 5 MHz focused transducer.

3.4.3 Attenuation evaluation in different directions

Copper specimens used in this test could be anisotropic. Thus, evaluating the attenuation of the blocks in different directions is of interest. Six copper blocks were chosen for this purpose, from the first batch, and their attenuation in all 3 directions was measured in immersion using the 5 MHz focused transducer.

The results obtained for three samples, 8426, 8420 and 8421, with respective grain size 286, 344 and 372 μm, for three directions referred to as H, L and W, respectively, are shown in Fig. 3.13. Since the heights of all the three blocks are smaller than their lengths and widths (cf Fig. 3.4), the attenuation curves (the solid curves) in the H-direction have broadest effective frequency ranges, e.g. approx. 0.5 - 1.9 MHz for Block 8426 (Fig. 3.13(a)), 0.5 - 2.5 MHz for Block 8420 (Fig. 3.13(b)), and 0.5 - 2.3 MHz for Block 8421 (Fig. 3.13(c)). Comparing the attenuation coefficients evaluated from the measurements performed in different directions (Fig. 3.13) one can see that the respective attenuation curves do not differ significantly in the effective frequency range. Conclusion can be drawn that the three blocks are very weekly anisotropic.

(a) Attenuation in Block 8426 (286 μ m)

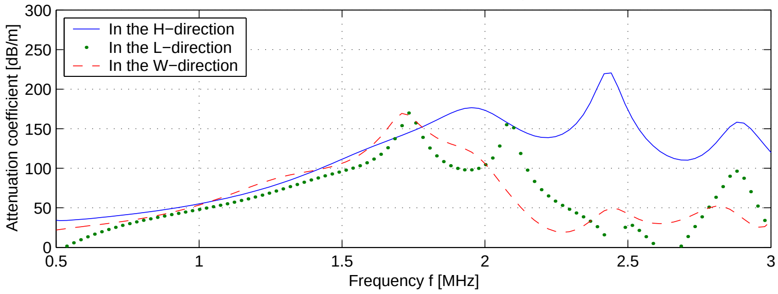

(b) Attenuation in Block 8420 (344 μ m)

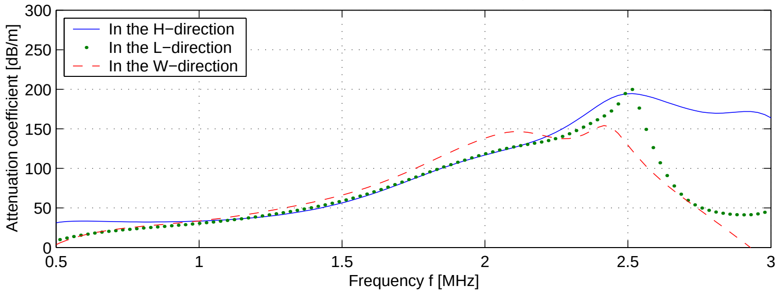

(c) Attenuation in Block 8421 (372 μ m)

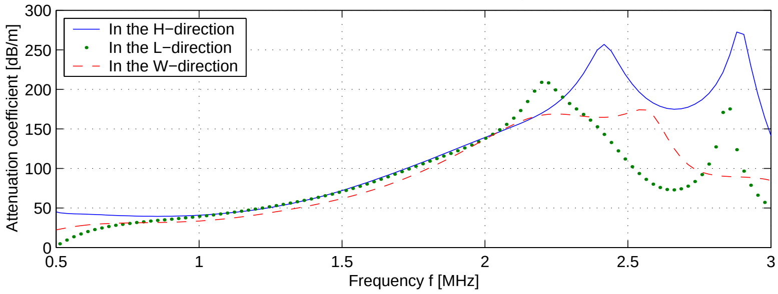

Figure 3.13: Attenuation coefficients in copper blocks with grains size of 286, 344 and 372 μm, evaluated in differnt directions using ALLIN system.

The results obtained for the specimens from batch 2 evaluated in the H- and W-directions (their H and W-dimensions are identical) are shown in Fig. 3.14. In this figure it can be seen that the attenuation in the H- and W-directions are quite different for Cu197, but only slightly different for Cu282. This reveals that the specimen Cu197 presents a significant anisotropy while the specimens Cu214 and Cu282 are only slightly anisotropic.

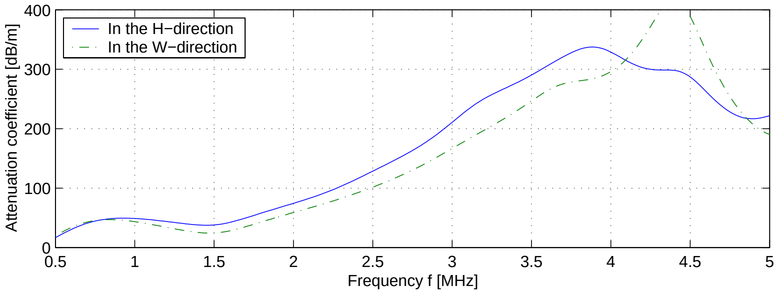
(a) Attenuation in Cu197 (197 µ m)

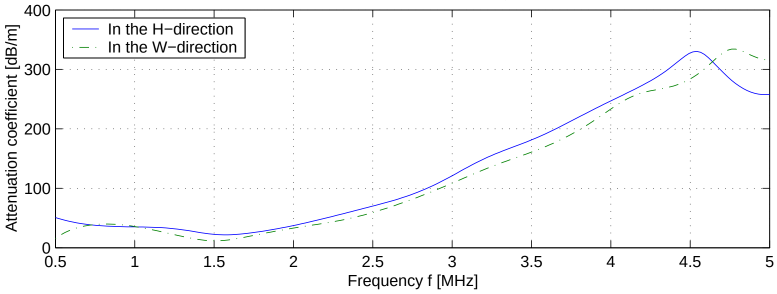
(b) Attenuation in Cu214 (214 µ m)

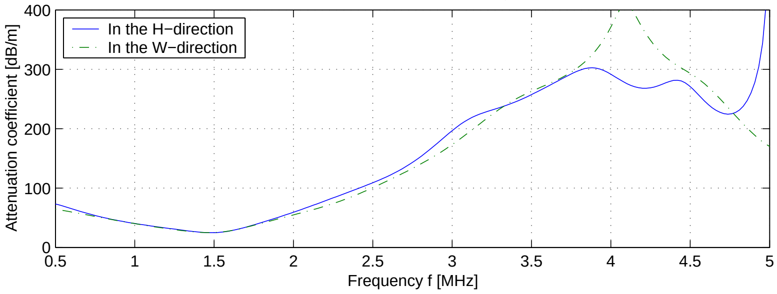
(c) Attenuation in Cu282 (282 µ m)

Figure 3.14: Attenuation coefficients in the specimens from batch 2 evaluated in the H-, L- and W-direction using RITEC system.

3.4.4 Attenuation using RITEC system and the planar 2.25 MHz transducer

Attenuation evaluation was also conducted using a planar transducer PANAMETRICS V325 with a nominal Frequency of 2.25 MHz and a diameter of 10 mm. In this case diffraction correction was performed using the procedure presented in Section 3.2.3, and in detail in Appendix 3.A.

The attenuation values without the correction were obtained using Eqs. (3.2) and (3.6), and with diffraction correction, using Eqs. (3.15), (3.16), (3.17), and (3.14), respectively. Comparison of the results obtained without and with diffraction correction is shown in Fig. 3.15. The diffraction correction curves (the difference of the resulting attenuation as a function of frequency) for the blocks with 81 and 299 μm are shown in Fig. 3.16. Small difference between the curves can be observed due to the nonlinear way of introducing the correction into Eq. (3.15), which makes the corrected result dependent on the measurements. From Fig. 3.16 it can be seen that the error caused by the diffraction loss is large, ranging from 40 to 50 dB/m in the frequency from 0.5 to 3.5 MHz. Therefore, diffraction correction is necessary for any planar transducer used to measure thick copper blocks (e.g., a 60 mm thickness in the present case).

(a) Attenuation evaluation without diffraction correction (RITEC)

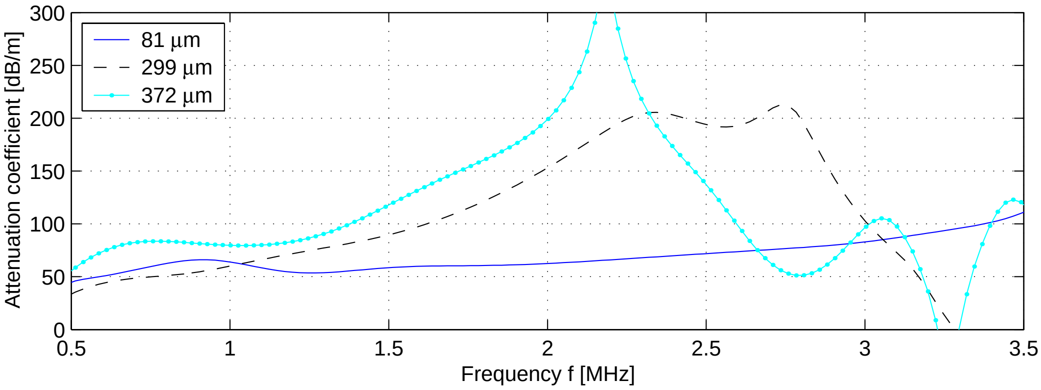

(b) Attenuation evaluation with diffraction correction (RITEC)

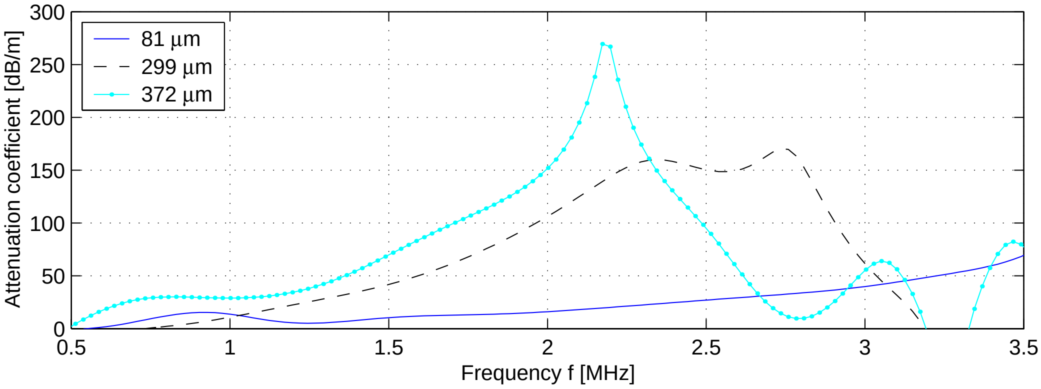

Figure 3.15: Comparison of attenuation coefficients from 2.25-MHz planar transducer without and with diffraction correction.

Results obtained with the planar transducer, respectively, without and with diffraction correction can be compared with those from the focused transducer for the copper blocks with 81 and 344 μm, in Figs. 3.17 and 3.18, respectively. The comparison shows, as expected, that the attenuation obtained using the planar transducer without diffraction correction is much overestimated and higher than that from the focused transducer. After diffraction correction the attenuation values are lower than the respective values for focused transducer, which is also

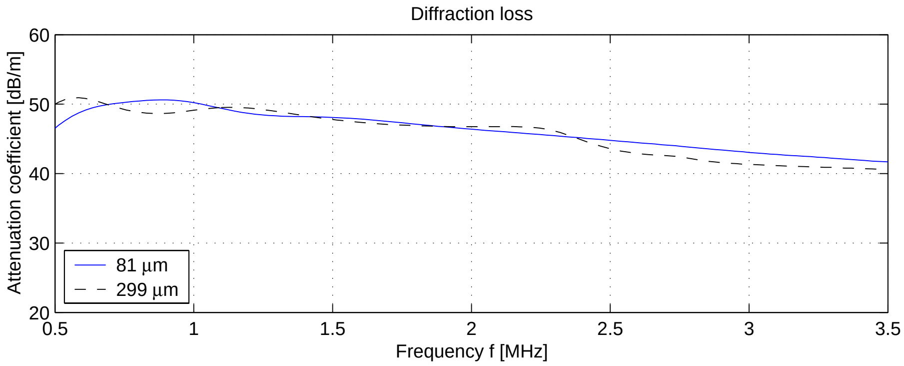

Figure 3.16: Diffraction correction for 2.25-MHz planar transducer with a 10 mm diameter.

expected since the focused transducer introduces small diffraction losses that depend on its focal distance and its water path above the inspected surface.

Generally, using focused transducers enables measurements on thick samples of attenuating materials but may yield inaccurate results while application of planar transducers facilitates diffraction correction but cannot be applied for thick samples.

It should be also noted that in the immersion method the parallelism of the transducer's and sample's surfaces has significant influence on the evaluation precision. To minimize this error, a level-meter was used in combination with observing the B-scans of the sample's front surfaces.

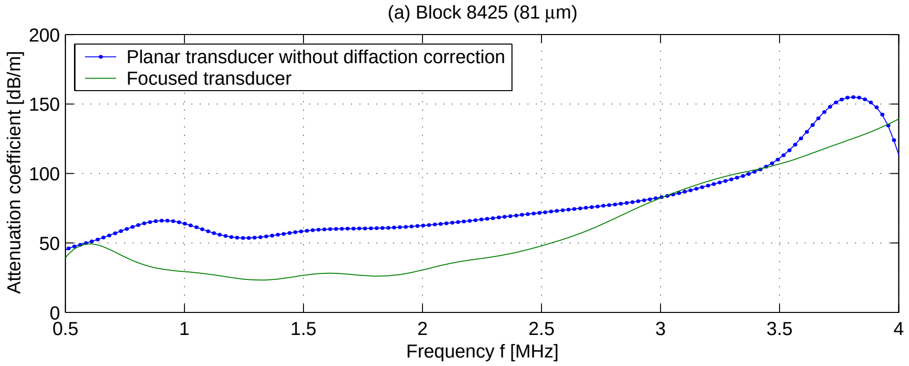

(b) Block 8425 (81 µm)

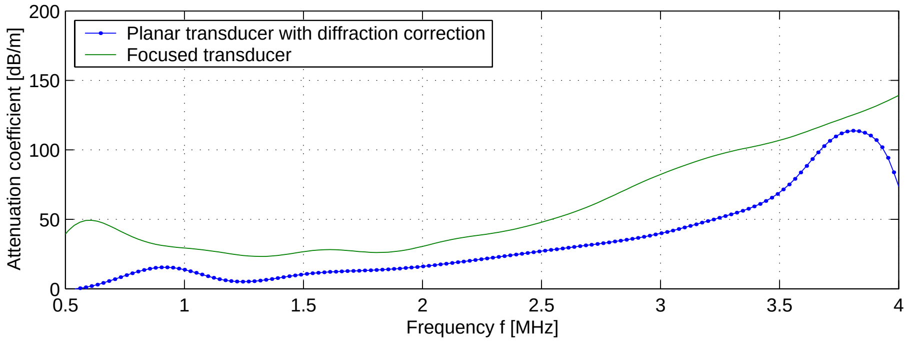

Figure 3.17: Comparison of attenuation coefficients from focused transducer and 2.25-MHz planar transducer without and with diffraction correction.

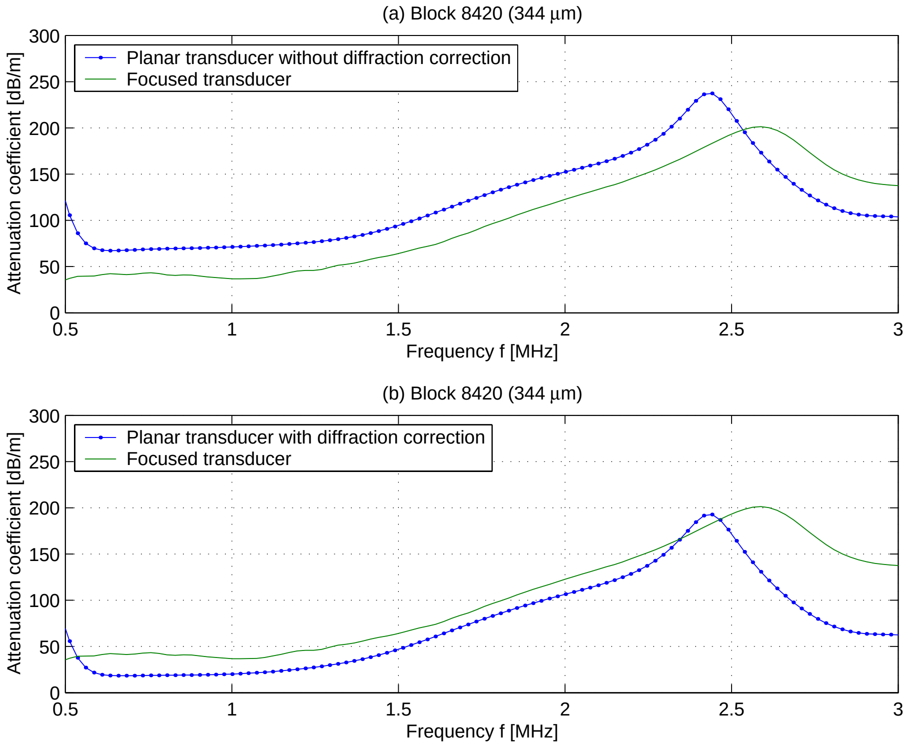

Figure 3.18: Comparison of attenuation coefficients from focused transducer and 2.25-MHz planar transducer without and with diffraction correction.

3.4.5 Effects of attenuation on ultrasonic detection of defects

The effects of attenuation on ultrasonic detection of defects were investigated using ALLIN system with the 5MHz focused transducer from Panametrics. The water path was about 25 mm which resulted in the focus at a depth of approx. 54 mm in copper block. The measurements were made on the batch 1 where all specimens had four FBHs. In Fig. 3.19 the C-scans containing images of the four FBHs with diameters of 1, 2, 3 and 4 mm are presented.

The 3 mm and 4 mm FBHs are clearly seen in all the C-scans in Fig. 3.19; the 2 mm FBHs are clearly visible for most blocks, but a little difficult to distinguish from grain noise for the specimens with the latgest grains, that is the 8426 (286 μm), the 8422 (305 μm), and the 8421 (372 μm). The 1 mm holes are only slightely pronounced in the C-scans of blocks 8425 (81 μm) and 8423 (112 μm) (although they are difficult to see in the figure). Therefore, the 1 mm FBHs could not be used in the present study of defect detectability. The most appropriate signals used for reliable estimation of signal to noise were those from the 4 mm FBHs.

In the study of the detectability of an ultrasonic NDE system, the signal-to-noise ratio (SNR) as a function of grain size and attenuation was investigated. The SNR is calculated from the following relation

$$SNR = \frac{estimated\ amplitude\ of FBH's\ echo}{3 \cdot (standard\ deviation\ of\ grain\ noise)} \tag{3.18}$$

To evaluate the standard deviation (or the square root of variance) of grain noise, special C-scans were created from the recorded three dimensional data which contain full RF signals at the depth of FBHs. In these C-scans, the middle regions between the four FBHs were selected and then their standard deviations were calculated.

The SNR is plotted as a function of grain size in Fig. 3.20, from which one can see that none

(a) Block 8425 (81 µm) (b) Block 8423 (112 µm)

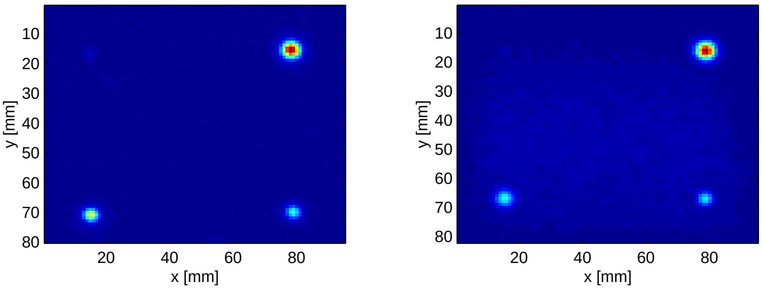

(c) Block 8426 (286 µm) (d) Block 8428 (299 µm)

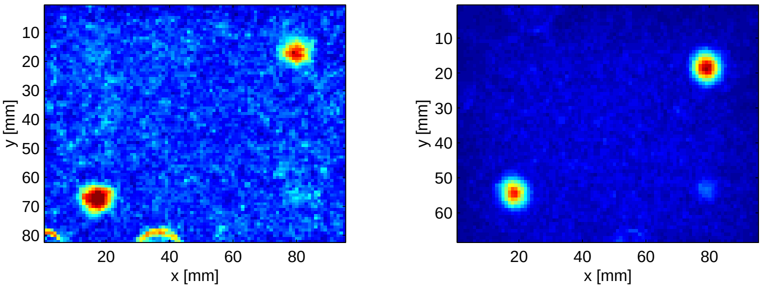

(e) Block 8422 (305 µm) (f) Block 8429 (320 µm)

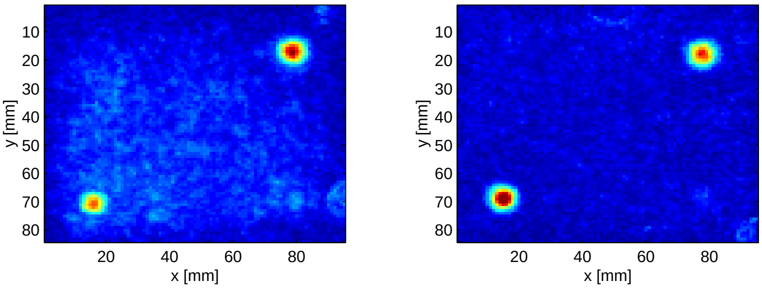

(g) Block 8424 (322 µm) (h) Block 8420 (344 µm)

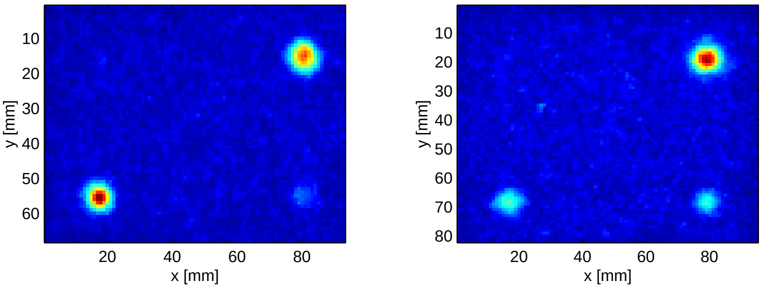

(i) Block 8427 (366 µm) (j) Block 8421 (372 µm)

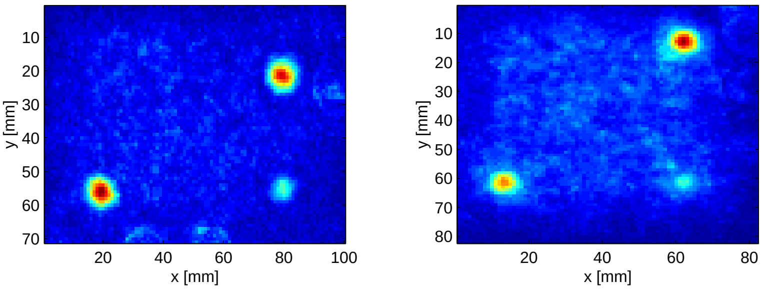

Figure 3.19: C-scans of the flat bottom holes in specimens from batch 1. Hole diameters 1, 2, 3 and 4 mm are located at the upper left, lower right, lower left and upper right corners, respectively.

of the three SNR-Grain-size curves shows clear correlation of the measured SNR with grain size. Interestingly, the 286 μm which was a clear outlier in the attenuation plots (cf Fig. 3.10) is characterized by the lowest SNR for all hole diameters. Moreover, the SNR measured for the largest hole diameter (most reliable) shows clear correlation with the attenuation measurements presented in Fig. 3.10; the 366 μm specimen has lower SNR than the 372 μm one and the similarity between the results for 320 μm and 322 μm is also pronounced. This indicate that the SNR is more correlated with the attenuation than the grain size.

This relation can be also observed in Fig. 3.21 where the SNR is presented as a function of attenuation. In this case, the SNR-attenuation curve for the 4 mm FBH (in the lower panel) shows a monotonic decrease of the SNR with attenuation, except a clear outlier for $\alpha = 82$ dB/m/MHz corresponding again to the 286 μm specimen.

It should be noted that roughness and flatness of the FBH's bottoms manufactured using drilling/milling operations have affected the amplitudes of the respective echoes and in this way impaired accuracy of the SNR measurements. More proper would have been manufacturing those holes using the electrical discharge method which is recommended in the next measurements of this type.

Based on the above results we can draw conclusion that for the samples in batch 1 defect detecteability is stronger correlated with the attenuation than the grain size.

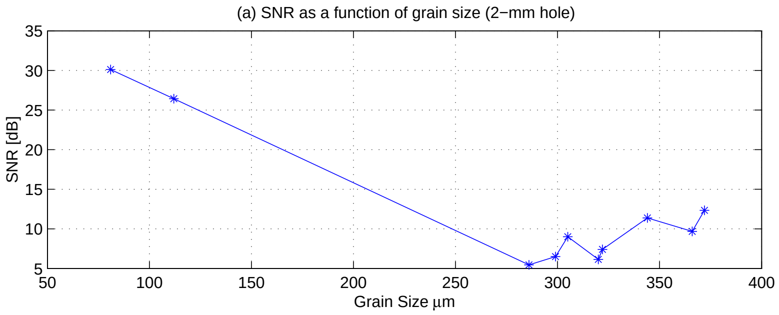

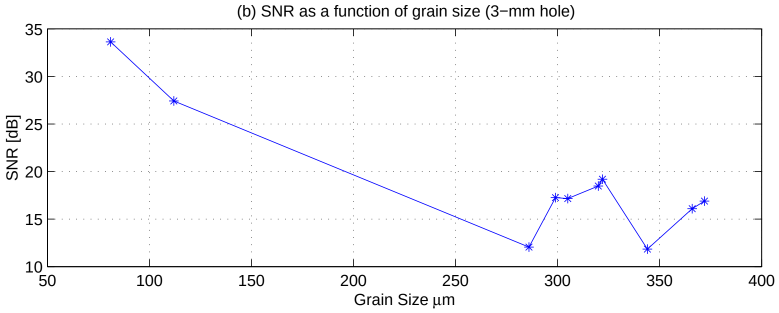

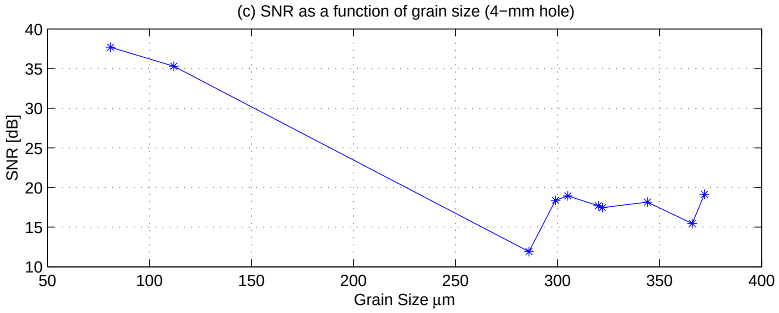

Figure 3.20: SNR of the FBH echoes as a function of grain size.

(a) SNR as a function of attenuation (2−mm hole)

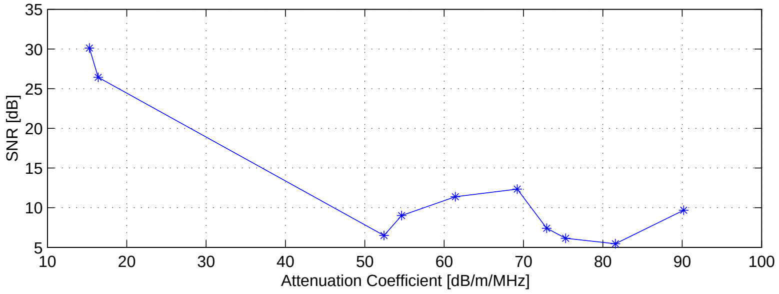

(b) SNR as a function of attenuation (3−mm hole)

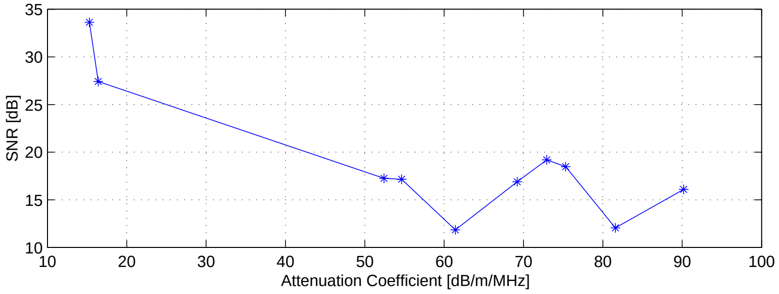

(c) SNR as a function of attenuation (4−mm hole)

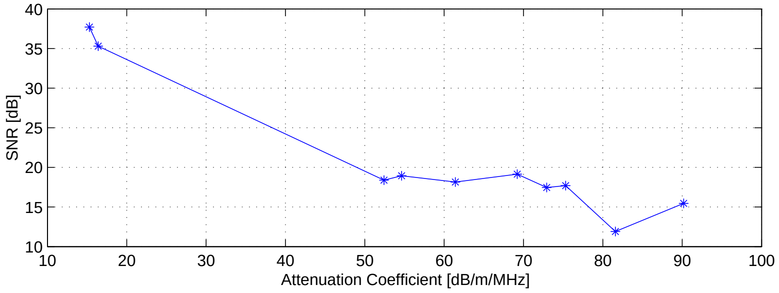

Figure 3.21: SNR of the FBH echoes as a function of Attenuation.

3.5 Conclusions

Attenuation of 13 copper blocks with different grain size has been evaluated using immersion method (IM). Two ultrasonic setups were used in the measurements: the RITEC instrument with the digital oscilloscope from Agilent as a reference, and the industrial digital system ALLIN. Two different transducers were applied, the focused and the planar transducer from Panametrics.

The calculation of diffraction loss for the planar transducer was implemented in MATLAB and an automatic frequency dependent diffraction correction was applied in the attenuation evaluation.

The results have shown that the attenuation is a nonlinear function of frequency, and that the copper blocks with fine grains, generally have smaller attenuation than those with large grains. However, the results (Fig. 3.10) also show an inconsistence between attenuation and grain size, that is, some blocks with smaller grains have larger attenuation than those with larger grains.

The results obtained from the RITEC and ALLIN systems with the focused transducer and the planar transducer (before and after diffraction correction) were compared. The comparison shows that the evaluated results from the RITEC and ALLIN systems with the same transducer were in good agreement.

Generally, the attenuation measured both with planar and focused transducer is overestimated but measurements performed with focused transducer were quite close to those obtained with planar transducer after diffraction correction.

The attenuation measured for ten blocks with the grains from 81- to 372 μm ranges from 30 to 180 dB/m at frequency 2.0 MHz, and from 39 to 221 dB/m at frequency at 2.25 MHz.

The effect of grain size on the defect detectability was investigated by inspecting quasi-flat bottom holes (FBHs) of different diameters in 10 copper specimens with different grain size. The SNR estimated for holes echoes were analyzed in terms of both grain size and attenuation. The results demonstrate that the SNR is stronger correlated with the evaluated ultrasonic attenuation in the respective blocks than with their grain size.

Attenuation of six selected copper blocks was also evaluated using ultrasonic waves propagating in different directions to check if the blocks were anisotropic. The results of the evaluation demonstrate that the attenuation coefficients in five specimens are similar, while one specimen shows noticeable anisotropy.

Some interesting topics for further work:

- design a portable, handheld instrument for attenuation estimation based on the buffer rod method
- develop means for the diffraction correction of focused transducers
- investigate the influence of transducer bandwidth on the accuracy of attenuation estimation

Bibliography

[1] ASTM E 664-93. *Standard Practice for the Measurement of the Apparent Attenuation of Longitudinal Ultrasonic Waves by Immersion Method.* ASTM International, www.astm.org/DATABASE.CART/REDLINE_PAGES/E664.htm, 2005.

[2] ASTM C 1332-01. *Standard Test Method for Measurement of Ultrasonic Attenuation Coefficients of Advanced Ceramics by Pulse-Echo Contact Technique.* ASTM International, www.astm.org/DATABASE.CART/REDLINE_PAGES/C1332.htm, 2005.

[3] WN. Reynolds R.L. Smith and H.N.G. Wadley. Ultrasonic attenuation and microstructure in low-carbon steels. *Met. Sci.*, 15:554–558, 1981.

[4] E. P. Papadakis. *Scattering in polycrystalline media, in Methods of experimental physics: – Ultrasonics, ed. P.E. Edmonds*, volume 19, pages 237–299. Academic Press, New York, 1981.

[5] E. P. Papadakis. *Ultrasonic attenuation caused by scattering in polycrystalline media, in Physical Acoustics, ed. W.P. Mason*, volume 4 Part B, pages 269–328. Academic Press, New York, 1968.

[6] R.L. Granato and K. Lücke. Theory of mechanical dampling due to dislocations. *J. appl. Phys.*, 27(6):583–593, June 1956.

[7] K. Lücke. Theory of mechanical dampling due to dislocations. *J. appl. Phys.*, 27(12):1433–1438, December 1956.

[8] E. P. Papadakis. Ultrasonic attenuation in thin specimens drivrn through buffer rods. *J. Acoust. Soc. Am.*, 44(3):724–734, 1968.

[9] E. P. Papadakis. Buffer-rod system for ultrasonic attenuation measurements. *J. Acoust. Soc. Am.*, 44(5):1437–1441, 1968.

[10] E. P. Papadakis, K. A. Fowler, and L. C. Lynnworth. Ultrasonic attenuation by spectrum analysis of pulses in buffer rods: Method and diffraction corrections. *J. Acoust. Soc. Am.*, 53:1336–1343, 1973.

[11] E. P. Papadakis. *Ultrasonic velocity and attenuation: measurement methods with scientific and industrial applications, in Physical Acoustics, edited by W.P. Mason and R.N. Thurston*, volume 12, pages 277–374. Academic Press, New York, 1976.

[12] E. P. Papadakis. *Ultrasonic attenuation caused by scattering in polycrystalline media, in Physical Acoustics, ed. W.P. Mason*, volume 4 Part B, pages 269–328. Academic Press, New York, 1976.

[13] E. P. Papadakis. *The measurement of ultrasonic attenuation, in Physical Acoustics, edited by R.N. Thurston, and A.D. Pierce*, volume 19, pages 107–155. Academic Press, San Diego, 1990.

[14] P.B. Nagy and L. Adler. Scattering induced attenuation of ultrasonic backscattering. *Rev. of Progr. in Quantitative NDE.*, 7:1263–1271, 1988.

[15] P. Wu, F. Lingvall, and T. Stepinski. Inspection of copper canisters for spent nuclear fuel by means of ultrasonic array system - electron beam evaluation, modelling, and materials characterization. Technical Report TR-99-43, SKB, 1999.

[16] P. Wu, F. Lingvall, and T. Stepinski. Inspection of copper canisters for spent nuclear fuel by means of ultrasound - electron beam evaluation, harmonic imaging, materials characterization and ultrasonic modelling. Technical Report TR-00-23, SKB, 2000.

[17] L. E. Kinsler, A. R. Frey, A. B. Coppens, and J. V. Sanders. *Fundamentals of Acoustics.* John Wiley & Sons, New York, 3rd edition, 1982.

[18] Jr. M. A. Breaseale, J. H. Cantrel and J. S. Heyman. *Ultrasonic wave velocity and attenuation measurements, in Methods of experimental physics: – Ultrasonics, ed. P.E. Edmonds*, volume 19, pages 67–135. Academic Press, New York, 1981.

3.A Theory of the methods for attenuation evaluation

3.A.1 General consideration

The buffer rod method (BRM) and the immersion method (IM) use the the same theory. In both methods an intermediate medium between the transducer and the inspected sample is placed, the reflections (echoes) from the sample's front and back surfaces are used for the evaluation of attenuation (see Figs. 3.1 and 3.2). In attenuation evaluation, the reflection and transmission coefficients for plane waves are used which may lead to some error. Both methods require parallel surfaces in the buffer as well as in the sample. The difference of the two methods lies in that the BRM has the back surface in air whereas the IM has the back surface in the immersing fluid so that the reflection from the back surface in the IM is not assumed to be ideal (meaning total reflection) as in the BRM.

Here, we present a general the theory which applies for any case when the sample's back surface may have contact with any material, such as, air, water, or any other fluid or solid.

Referring to Fig. 3.1, we assume that the acoustic impedances of the buffer rod and the sample are Z_b and Z_s, respectively. Then, the reflection coefficients at the buffer/sample interface and the sample/buffer interface, $R_{bs} \equiv R$ and R_{sb}, can be written, respectively, as (Chap. 6 in [17])

$$R = R_{bs} = \frac{Z_s - Z_b}{Z_s + Z_b} \tag{3.19}$$

$$R_{sb} = \frac{Z_b - Z_s}{Z_b + Z_s} = -R \tag{3.20}$$

and the transmission coefficients at the buffer/sample and the sample/butter interfaces, T_{bs} and T_{sb}, can be expressed, respectively, as

$$T_{bs} = \frac{2Z_s}{Z_b + Z_s} \tag{3.21}$$

$$T_{sb} = \frac{2Z_b}{Z_s + Z_b} \tag{3.22}$$

From Eqs. (3.19) to (3.22) it is easy to find that

$$T_{bs}T_{sb} = 1 - R^2 \tag{3.23}$$

Furthermore, letting R_{back} be the reflection coefficient at the sample's back interface, and assuming that the incident wave has an amplitude of $I = I(f)$ at frequency f and the sample has an attenuation α in Nepers/m, we may find the front reflection from the sample's front surface, $A = A(f)$,

$$A = IR \tag{3.24}$$

the back reflection from the sample's back surface, $B = B(f)$,

$$\begin{aligned} B &= IT_{bs}R_{back}T_{sb}e^{-2\alpha L_s} \\ &= I(1 - R^2)R_{back}e^{-2\alpha L_s} \end{aligned} \tag{3.25}$$

and the 2nd back reflection from the back surface (noting the relation $R_{sb} = -R$ in Eq. (3.20)), $C = C(f)$,

$$\begin{aligned} C &= IT_{bs}R_{back}R_{sb}R_{back}T_{sb}e^{-4\alpha L_s} \\ &= -IR(1 - R^2)R_{back}^2 e^{-4\alpha L_s} \end{aligned} \tag{3.26}$$

The ratio of the front echo and the back echo follows from Eqs. (3.24) and (3.25)

$$\tilde{A} = \frac{A}{B} = \frac{R}{(1-R^2)R_{back}e^{-2\alpha L_s}} \tag{3.27}$$

The ratio of the first back echo and the second back echo can be written, from Eqs. (3.25) and (3.26), as

$$\tilde{B} = \frac{B}{C} = \frac{1}{-RR_{back}e^{-2\alpha L_s}} \tag{3.28}$$

It should be pointed out that in the present report $\tilde{B}$ is used instead of $\tilde{C} = C/B$ that is used in references [8–13, 18]. From $\tilde{A}/\tilde{B} = -R^2/(1-R^2)$, we can find the reflection coefficient from A and B (that are available from measurements), as follows

$$R = \sqrt{\frac{\tilde{A}/\tilde{B}}{\tilde{A}/\tilde{B} - 1}} \tag{3.29}$$

When R is determined, the corrected attenuation coefficient can be found from Eq. (3.28) as follows

$$\alpha = \frac{1}{2L_s} \ln \left[-RR_{back}\tilde{B} \right] \tag{3.30}$$

where α is in nepers/m. In terms of dB/m, Eq. (3.30) can be expressed as

$$\alpha = \frac{1}{2L_s} 20 \log_{10} \left[-RR_{back}\tilde{B} \right] \tag{3.31}$$

It is easy to find that 1 Nepers = 8.6858 dB. An alternative form to find the attenuation coefficient α can be obtained from Eq. (3.27),

$$\alpha = \frac{1}{2L_s} \ln \left[\frac{(1-R^2)R_{back}}{R} \tilde{A} \right] \tag{3.32}$$

which, in terms of dB/m, can be written as

$$\alpha = \frac{1}{2L_s} 20 \log_{10} \left[\frac{(1-R^2)R_{back}}{R} \tilde{A} \right] \tag{3.33}$$

Re-writing Eqs. (3.31) and (3.33) in the following manner,

$$\alpha = \frac{1}{2L_s} 20 \log_{10} \left[-RR_{back} \right] + \frac{1}{2L_s} \left[20 \log_{10}(B) - 20 \log_{10}(C) \right] \tag{3.34}$$

$$\alpha = \frac{1}{2L_s} 20 \log_{10} \left[\frac{(1-R^2)R_{back}}{R} \right] + \frac{1}{2L_s} \left[20 \log_{10}(A) - 20 \log_{10}(B) \right] \tag{3.35}$$

we can easily find that the buffer rod method is essentially the logarithmic spectral difference method that takes into account the reflection from the front and back interfaces. Eq. (3.34) is the logarithmic spectral difference method based on the spectra of the 1st back and 2nd back echoes for broad band measurement. Eq. (3.35) is the logarithmic spectral difference method based on the spectra of the front and 1st back echoes.

3.A.2 Buffer rod method

If the back surface is in air, then it is reasonable to assume $R_{back} \approx -1$, which means a total reflection from the back surface. In this case, Eq. (3.31) becomes

$$\alpha = \frac{1}{2L_s} 20\log_{10}\left[R\tilde{B}\right] \tag{3.36}$$

which is the existing buffer rod method. Eq. (3.33) becomes

$$\alpha = \frac{1}{2L_s} 20\log_{10}\left[\frac{-(1-R^2)}{R}\tilde{A}\right] \tag{3.37}$$

3.A.3 Immersion method

In the immersion inspection, $R_{back} = R_{sb} = -R$. In this case, Eq. (3.30) reduces to

$$\alpha = \frac{1}{2L_s} 20\log_{10}\left[R^2\tilde{B}\right] \tag{3.38}$$

which is different from that in the existing buffer rod method. Therefore, in the immersion inspection, one should use Eq. (3.38) instead of Eq. (3.36).

Eq. (3.33) reduces to

$$\alpha = \frac{1}{2L_s} 20\log_{10}\left[-(1-R^2)\tilde{A}\right] \tag{3.39}$$

Misusing Eq. (3.36) in the immersion method will result in some estimate error, especially when the acoustic impedances of the sample and the immersing fluid differ not so much (e.g., for polystyrene immersed in water, the acoustic impedance of the polystyrene is only 1.68 times that of water so that $R = 0.2530$, and $R^2 = 0.0640$. In this case Eq. (3.36) gives an error of $20\log_{10}(0.2530)$ = -11.94 dB).

3.A.4 Diffraction correction

The diffraction of a transducer will be one of the main sources causing error in attenuation estimation, especially when the BRM and IM are used to evaluate attenuation for thick materials. The loss due to diffraction (or beam spreading) will result in apparent "attenuation". The correction of this error, known as diffraction correction, was made presently only for planar transducers. To realize the diffraction correction, one needs to calculate diffraction loss (DL). For planar circular transducer, one normalized DL curve like in Fig. 3.3 is sufficient for correcting diffraction error for transducers with different radii at different frequencies. When the DL curve is available, the diffraction correction can be made using the following procedure.

First, determine the distances of the front interface echo, the 1st and the 2nd back interface echoes, which are normalized by $z_b = a^2/\lambda_b$ in the buffer and $z_s = a^2/\lambda_s$ in the sample,

$$S_A = \frac{2L_b}{z_b} = \frac{2L_b}{(a^2/\lambda_b)} = \frac{2L_b c_b}{a^2 f} \tag{3.40}$$

$$S_B = \frac{2L_b}{z_b} + \frac{2L_s}{z_c} = \frac{2L_b}{(a^2/\lambda_b)} + \frac{2L_s}{(a^2/\lambda_s)} = \frac{2L_b c_b}{a^2 f} + \frac{2L_s c_s}{a^2 f} \tag{3.41}$$

$$S_C = \frac{2L_b}{z_b} + \frac{4L_s}{z_c} = \frac{2L_b}{(a^2/\lambda_b)} + \frac{4L_s}{(a^2/\lambda_s)} = \frac{2L_b c_b}{a^2 f} + \frac{4L_s c_s}{a^2 f} \tag{3.42}$$

where $\lambda_b = c_b/f$ and $\lambda_s = c_s/f$ are the wave lengths, and c_b and c_s are the sound speeds in the buffer and the sample, respectively.

Secondly, get the DL values in the DL curve in Fig. 3.3 at the above three distances S_A, S_B and S_C, and then use the following relations to compensate for diffraction loss for all the echoes' amplitudes, A, B and C,

$$A_c = A \cdot 10^{DL_A/20} \tag{3.43}$$

$$B_c = B \cdot 10^{DL_B/20} \tag{3.44}$$

$$C_c = C \cdot 10^{DL_C/20} \tag{3.45}$$

Finally, for BRM, substitute DL_A, DL_B and DL_C for A, B, C in Eqs. (3.29), (3.36) and (3.37), and get the corrected attenuation coefficient

$$\tilde{\alpha} = \frac{1}{2L_s} 20 \log_{10} \left(R_c \tilde{B}_c \right) \tag{3.46}$$

and the alternative form

$$\tilde{\alpha} = \frac{1}{2L_s} 20 \log_{10} \left[\frac{-(1 - R_c^2)}{R_c} \tilde{A}_c \right] \tag{3.47}$$

and for IM, substitute DL_A, DL_B and DL_C for A, B, C in Eqs. (3.29), (3.38) and (3.39), and get the corrected attenuation coefficient

$$\tilde{\alpha} = \frac{1}{2L_s} 20 \log_{10} \left(R_c^2 \tilde{B}_c \right) \tag{3.48}$$

and the alternative form

$$\tilde{\alpha} = \frac{1}{2L_s} 20 \log_{10} \left[-(1 - R_c^2) \tilde{A}_c \right] \tag{3.49}$$

where

$$R_c = \sqrt{\frac{\tilde{A}_c / \tilde{B}_c}{\tilde{A}_c / \tilde{B}_c - 1}} \tag{3.50}$$

$$\tilde{A}_c = \frac{A_c}{B_c} \tag{3.51}$$

$$\tilde{B}_c = \frac{B_c}{C_c} \tag{3.52}$$

ISSN 1404-0344
CM Digitaltryck AB, Bromma, 2006